

4. Discussion

The simplified ECD (equilibrium-control-dynamics) model when adjusted by experimental data can reproduce the time evolution of the position control. However, it is desirable that the adjusting parameters be calculated with only the design information for the device. Thus, the model will be used for the control system design. Four aspects of the application of this model will be discussed in detail. First, the methods used to determine those parameters will be discussed. Second, where the vacuum vessel is regarded as many loops of filament-current-coils (FCCs), the FCC approximation seems to have difficulty in reproducing the plasma ECD for the JT-60 tokamak with thick vacuum vessel sectors and thin bellows. The difficulty and the reason this method is still often used in many applications also will be described. Third, the influence of the eddy current field induced by the plasma motion on the position measurement will be discussed. Finally, the limitations of the simplified ECD model will be listed.

(1) Determining parameters in the simplified ECD model

The parameter θ relates to the ratio of OH (ohmic heating) coil flux dissipation. $\theta=0.7$ means that 70% of the flux (voltage-second) is consumed resistively in the plasma and conductors. The remainder (30%) is stored magnetically inside the plasma ring and will be returned to the PF (poloidal field) coil power supplies at the end of the discharge. Though this value must depend on the plasma internal quantities such as current profile, electrical resistance, etc., and thus it must change shot by shot, it seems to be a constant at the plasma current flat top in the discharge pulse. The constant value, θ , may be determined by the combination of the plasma internal states and current control dynamics and it is, therefore, still debatable how to determine θ . However, this is not pursued further in this chapter because θ has only a small influence on the ECD.

The parameter α (in $\kappa^{-\alpha}$ of Eq. (3.23)) is understood to be the volume effect in Shafranov's equilibrium equation. In this sense, this value depends on the distributions of the B_z field and plasma current density. The former is determined by the device VF (vertical field) coil location. Consequently, α is regarded as a parameter unique to the device itself with assumption of invariant current profiles.

The parameters k_R and k_Z are proportional coefficients of the relation between the magnetic field \mathbf{B} and plasma movement through eddy currents in the vessel. The relation of $\mathbf{B}\cdot\mathbf{v}_p$ is expressed as^[9]

$$\mathbf{B} = k_{cal} \cdot I_p \cdot \mathbf{v}_p, \quad (4.1)$$

$$k_{cal} \equiv \mu_0 \cdot \tau / (4\pi^2 a^2), \quad (4.2)$$

where the eddy current in the conductor is approximated by the surface current on the cylindrical conductor, τ is the time constant of the resistive conductor and a is the radius of the cylindrical conductor. Time constant of the doughnut-shaped vessel is taken as τ ;

$$\tau=L/R, \quad (4.3)$$

where L and R are the inductance and electrical resistance, respectively. They are given by

$$L=\mu_0 R_v \{\log(8R_v/a_v)-2\}, R=2\pi R_v/(2\pi a_v d\sigma), \quad (4.4)$$

where R_v and a_v are the major and minor radii of the vessel, respectively, d is the thickness of the vessel conductor and σ is the electrical conductivity. Then, k_{cal} is calculated by substituting the following JT-60 parameters for the variables in Eq. (4.2); $a=a_v=1.0$ m, $R_v=3.0$ m, $d=6.5$ cm (thick conductor parts) and $\sigma=7.69 \times 10^5 \Omega^{-1}m^{-1}$. $k_{cal}=2.36 \times 10^{-9}$ T/(A·m/sec). Taking into account the surface area of the thick sector parts ($=7/9$), $k_{cal}=1.8 \times 10^{-9}$ T/(A·m/sec), which is very close to the adjusted k values; $k_R=1.6 \times 10^{-9}$ T/(A·m/sec), $k_Z=1.3 \times 10^{-9}$ T/(A·m/sec). Even such an estimate made with cylindrical geometry can give the proper k value for the tokamak geometry. An analytical formula like Eq. (4.2) using the calculation of $\mathbf{H}(\mathbf{r})$ in Eq. (3.18) in tokamak geometry could give a more precise estimate of the k value.

Another method of estimating k is to solve an eddy current problem using tokamak geometry by the $\mathbf{A}-\phi$ method in the following way; (a) a plasma is assumed to be a set of multiple filament current coils, (b) by moving the plasma forcibly from the center of the vessel several times with a different plasma velocity, the magnetic field resulting from the eddy currents in the structural conductors is calculated, and (c) k is obtained as a function of time, plasma current and velocities. No dependency on plasma current and velocity is expected and k is expected to reach a constant quickly after motion begins.

The parameter τ can be also estimated by the eddy current analysis based on the $\mathbf{A}-\phi$ method. As mentioned in Section 2, the estimated τ_R through the bellows is less than 6.0 msec and that through the thick conductor part is ~ 15 msec, while the adjusted τ_R is 4.1 msec. This implies that the field penetrates the vessel through the bellows parts and actuates the plasma. An $\mathbf{A}-\phi$ calculation with a shorter discretized time step could give a more accurate value, but this requires a longer computation time than is presently available. (This remains a technical problem.)

Except θ , the parameters in the simplified ECD model can be estimated with only the design phase knowledge of the device. More microscopic refinements would be necessary to improve the estimate of θ .

(2) The issue of FCC approximation for a tokamak vessel

Analyses of a plasma have often adopted filament loop coils (FCCs) in place of the vacuum vessel. These analyses assume that the coil-vessel and plasma-vessel interactions are identical from the view of the characteristics of field propagation. Such an assumption is supported by a point that it makes the ECD system very simple; all coil-vessel-plasma interactions can be expressed as magnetic mutual couplings and the time evolution of the field can be easily obtained by solving a quasi-linear circuit equation. A part of the assumption, however, seems to be distorted in the toroidally non-uniform JT-60 tokamak. The plasma-vessel interactions can not be dealt with as mutual couplings like the relation of coils and vessel, because the plasma mass is negligibly small and even the small variations of magnetic field caused by the eddy currents in the vessel influence the plasma motion. Therefore, a plasma starts to move only when the magnetic field produced by the plasma current penetrates the vessel. In addition, a zero-inertia plasma always moves to maintain the balance of force. The magnetic field is induced instantly by the plasma motion in proportion to the plasma velocity, as mentioned in Section 3. On the other hand, in the FCC approximation the induced field is changed according to the system response of the coils (i.e. a vector first-order differential equation) and thus the field is not proportional to the plasma velocity. As the assumption of $m_p \cdot dv_p/dt = 0$ does not yield the velocity explicitly in FCC approximation, Newton's equation is required to be solved for velocity calculation. Only when the time constants of the FCCs are short enough and the electrical resistances are appropriately set, can the FCC approximation provide good results. This is now checked by calculating the parameter k in the FCC approximation: <1> 84 filament coils are used in place of the JT-60 vessel. Their electrical resistances are selected for two cases; the vessel made of the bellows & thick conductor parts and that made of only the thick conductor parts. <2> A filament current plasma is moved forcibly from the center of the vessel at constant velocities of 0.1 m/sec to 1.0 m/sec in the R_p and Z_p directions. k ($\equiv B(\text{at the plasma center})/(I_p \cdot v_p)$) values are obtained as a function of time, as shown in Fig. 4.1. The following interpretations are possible:

- (a) No dependency on the velocity in the approximation is observed.
- (b) The time constants in the bellows & thick conductor vessel are shorter than those in the thick conductor vessel but still longer than expected.
- (c) The saturated k values in the bellows & thick conductor vessel are much smaller than the actual k , while those in the thick conductor vessel are larger than the actual k .

It seems almost impossible to determine the appropriate inductances and resistances of the FCCs for the plasma-vessel interactions in the JT-60 tokamak. Even if the inductances and resistances are forcibly fitted for the plasma-vessel interactions, these values will not be compatible in the coil-vessel interactions.

Thus it is understood that FCC is not applicable to JT-60. Applicability of FCC to toroidally uniform tokamaks is also questionable, because most part of the discussion in Section 3 is effective in toroidally uniform geometry. It is necessary to verify the applicability of FCC to toroidally uniform tokamaks with experimental evidence.

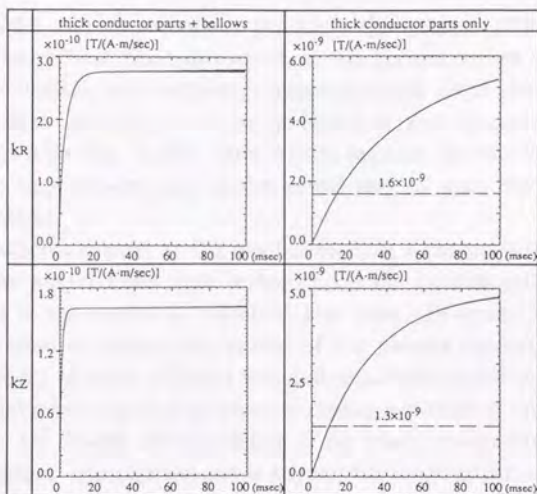


Fig. 4.1 Time Evolution of the Coefficient k in the Filament Current Approximation

(3) Influence of the plasma-induced eddy current on position measurement

The eddy current induced by the plasma motion is estimated using $I_p = 1.0$ MA and $v_p = 1.0$ m/sec in R_p and Z_p directions. $B_z^{\text{eddy}} = 0.0016$ T and $B_R^{\text{eddy}} = 0.0013$ T are obtained, while the magnetic field resulting from the plasma current is ~ 0.2 T at the sensors. Consequently, an error of $\sim 1\%$ is included in the measured field signals. The plasma position is calculated as the center of the outermost flux surface and the magnetic field corresponds to a gradient of the flux. Therefore, the error of the magnetic field is proportionally related to the distance between the plasma surface and the vessel wall. When the distance

is 0.1 m, the error is $\sim 1\%$ of 0.1 m, i.e. 1.0 mm, which is negligibly small in this discussion.

(4) Limitations of the simplified ECD model

Figures 3.2(a) through 3.2(h) in Section 3.3 have several limitations. These application limits of the simplified ECD model are as follows:

(a) The model cannot apply to a device whose PF coil field is not regarded to be uniform because the "one-point-representation of a plasma" such as R_p , Z_p , I_p , $B(R_p, Z_p)$ was adopted. This representation premises the fact that the vertical and horizontal magnetic field by the PF coil must uniformly act on the plasma column.

(b) The model cannot reproduce precisely the volume effect. Especially concerning the vertical position control, as the plasma moves away from the center of the vessel, the horizontal magnetic field B_r at the center of the plasma increases as a result of the feedback control to maintain constant velocity, shown in Fig. 3.2(h). This results because B_r decreases from the center to the upper/lower part of the vessel and so does the total force to actuate the plasma.

(c) Eddy currents caused by the displacement of a plasma with a current of -1 MA in the vessel have little influence on the equilibrium and position measurement in the model at velocities less than -10 m/sec. The simulated plasma is limited to around the period of the plasma current flat top. The combined model of eddy currents and full equilibria could reproduce more transient behavior of rapid displacement during a period of current ramp-up or disruption. Of course, the simulation of an entire plasma discharge would require the further investigation and is beyond the scope of this chapter.

5. Conclusions

The results of this study provide the following conclusions:

(1) The $A-\phi$ method with anisotropic conductivity can reproduce the evolution of the external field penetration into the JT-60 vessel. The penetration characteristics are determined by the bellows part. The penetration response is regarded as a system of a first-order differential equation. The accuracy of the $A-\phi$ method was evaluated by comparison with an analytical solution of a field penetration problem in the cylinder.

(2) The ITP (infinitely-thin-plate) and FCC (filament-current-coil) approximations for the vessel are not as accurate as the $A-\phi$ method to simulate JT-60 operations.

(3) The simplified ECD (equilibrium-control-dynamics) model can well reproduce the JT-60 position control. The parameters in the model can be determined by knowledge of the device available during the design phase. Thus, the model is able to be used for the design of the plasma feedback control system.

(4) It is improbable that the FCCs used in place of the vessel can simulate the plasma-vessel interaction in JT-60. The plasma-vessel interaction is explained by the characteristic that the equilibrium force on the plasma is balanced, and the approximate relation, $B_{move} = K \cdot I_p \cdot v_p$, holds.

References in Chapter III.1

- [1] Miya, K. and Nakata, T. (ed.), "Proceedings of the international workshop for eddy current code comparison," (Oct. 1986)
- [2] Ozeki, T. and Nakamura, Y., "Modal analysis of eddy current in JT-60 multi-torus system," Japan Atomic Energy Research Institute Report JAERI-M 83-159, (Oct. 1983)
Kameari, A. and Suzuki, Y., "Eddy current analysis by the finite element circuits," Japan Atomic Energy Research Institute Report JAERI-M 7120, (May 1977) (in Japanese)
- [3] Miya, K. et al., "Three dimensional analysis of an eddy current by the T-method," Proceedings of the IUTAM symposium(Tokyo Oct.1986), p.183
- [4] (for example)
Jardin, S.C. et al., "Dynamic modeling of transport and positional control of tokamaks," Journal of computational physics vol.66(1986) p.481
Lister, J.B. et al., "Experimental study of the vertical stability of high decay index plasmas in the DIII-D tokamak," General Atomics Co. report GA-A19843 (Feb. 1990)
- [5] Yokomizo, H. et al., "Equilibrium and axisymmetric stability of dee-shaped plasmas in Doublet III," Nuclear Fusion vol.22 (1982) p.797
- [6] Mukhovatov, V.S. and Shafranov, V.D., "Plasma equilibrium in a tokamak," Nuclear Fusion vol.11 (1971) p.605
- [7] Swain, D.W. and Neilson, G.H., "An efficient technique for magnetic analysis of non-circular, high-beta tokamak equilibria," Nuclear Fusion vol.22 (1982) p.1015
- [8] Kurihara, K. et al., "JT-60 plasma control system," Fusion Engineering and Design vol.11 (1990) p.441
- [9] Uchida, T. and Inoue, N., "Plasma control for magnetic nuclear fusion," the University of Tokyo Press (1982) (in Japanese)

Appendix Analytical solution of magnetic field penetration into an infinitely long cylindrical conductor

The magnetic field diffusion problem (Eq. (2.9)) in the infinitely long cylinder geometry (shown in Fig. 2.1) with an external filament current is classified in the pre-unfixed Dirichlet-boundary value problem for a parabolic partial differential equation. The formulation of the solution in the conductor is given as an infinite series of the Bessel-Fourier expansion.

$$Az(\rho, \theta, t) = \sum_{v=0}^{\infty} \sum_{\lambda=1}^{\infty} C_{v\lambda}(t) \cdot J_v(\omega_{v\lambda} \cdot \rho) \cdot \cos v\theta + \sum_{v=0}^{\infty} D_v(t) \cdot \left(\frac{\rho}{a}\right)^v \cdot \cos v\theta \quad (A.1)$$

where J_v is the v -th order Bessel function of the first kind, $C_{v\lambda}(t)$ and $D_v(t)$ are coefficients of the combination of eigenfunctions, $\omega_{v\lambda}$ is a constant of separation of variables and a is a radius of the outer-surface of the cylinder. $\omega_{v\lambda}$ is defined as $\omega_{v\lambda} \equiv \kappa \cdot \beta_{v\lambda} / (a-g)$, where $\beta_{v\lambda}$ is the λ -th zero point of J_v , i.e. $J_v(\beta_{v\lambda})=0$ and $\beta_{v\lambda} > 0$, g is a radius of the inner-surface of the cylinder and κ is a parameter to adjust a constant of separation of variables. By the integration of Eq.(2.9) with the imposing boundary conditions and the continuity conditions of the solution on the boundary, the following equations related to $C_{v\lambda}(t)$ and $D_v(t)$ are obtained. The complicated process to solve these equations is not described because this would distract from the purpose of this chapter.

$$\sum_{m=1}^{\infty} P_{v\lambda m}^* \cdot \frac{dC_{vm}}{dt} + Q_{v\lambda}^* \cdot \frac{dD_v}{dt} = \sum_{m=1}^{\infty} S_{v\lambda m}^* \cdot C_{vm} \quad (A.2)$$

$$\sum_{m=1}^{\infty} P_{vm}^{\#} \cdot \frac{dC_{vm}}{dt} + Q_v^{\#} \cdot \frac{dD_v}{dt} = \sum_{m=1}^{\infty} S_{vm}^{\#} \cdot C_{vm} + D_v + f_v(t) \quad (A.3)$$

$$\begin{aligned} P_{v\lambda m}^* &\equiv \frac{(a-g)^2}{\kappa^2 (\beta_{vm}^2 - \beta_{v\lambda}^2)} \left[a \cdot \left\{ \frac{\kappa \cdot \beta_{vm}}{a-g} J_{v+1} \left(\frac{\kappa \cdot \beta_{vm} \cdot a}{a-g} \right) \cdot J_v \left(\frac{\kappa \cdot \beta_{v\lambda} \cdot a}{a-g} \right) - \frac{\kappa \cdot \beta_{v\lambda}}{a-g} J_{v+1} \left(\frac{\kappa \cdot \beta_{v\lambda} \cdot a}{a-g} \right) \cdot J_v \left(\frac{\kappa \cdot \beta_{vm} \cdot a}{a-g} \right) \right\} \right. \\ &\quad \left. - g \cdot \left\{ \frac{\kappa \cdot \beta_{vm}}{a-g} J_{v+1} \left(\frac{\kappa \cdot \beta_{vm} \cdot g}{a-g} \right) \cdot J_v \left(\frac{\kappa \cdot \beta_{v\lambda} \cdot g}{a-g} \right) - \frac{\kappa \cdot \beta_{v\lambda}}{a-g} J_{v+1} \left(\frac{\kappa \cdot \beta_{v\lambda} \cdot g}{a-g} \right) \cdot J_v \left(\frac{\kappa \cdot \beta_{vm} \cdot g}{a-g} \right) \right\} \right] \quad (\lambda \neq m) \\ &\equiv \frac{a^2}{2} \left\{ J_v^2 \left(\frac{\kappa \cdot \beta_{v\lambda} \cdot a}{a-g} \right) - J_{v+1} \left(\frac{\kappa \cdot \beta_{v\lambda} \cdot a}{a-g} \right) \cdot J_{v-1} \left(\frac{\kappa \cdot \beta_{v\lambda} \cdot a}{a-g} \right) \right\} - \frac{g^2}{2} \left\{ J_v^2 \left(\frac{\kappa \cdot \beta_{v\lambda} \cdot g}{a-g} \right) - J_{v+1} \left(\frac{\kappa \cdot \beta_{v\lambda} \cdot g}{a-g} \right) \cdot J_{v-1} \left(\frac{\kappa \cdot \beta_{v\lambda} \cdot g}{a-g} \right) \right\} \quad (\lambda = m) \end{aligned}$$

$$\begin{aligned} Q_{v\lambda}^* &\equiv \frac{a-g}{\kappa \cdot a^v \cdot \beta_{v\lambda}} \left\{ a^{v+1} \cdot J_{v+1} \left(\frac{\kappa \cdot \beta_{v\lambda} \cdot a}{a-g} \right) - g^{v+1} \cdot J_{v+1} \left(\frac{\kappa \cdot \beta_{v\lambda} \cdot g}{a-g} \right) \right\}, & S_{v\lambda m}^* &\equiv - \frac{\kappa^2 \cdot \beta_{vm}^2}{\sigma_{\mu} \mu (a-g)^2} \cdot P_{v\lambda m}^* \\ P_{vm}^{\#} &\equiv \begin{cases} \frac{\sigma_{10}}{2} \cdot Q_{vm}^* \cdot \log \left(\frac{a^2}{\alpha} \right) & (v=0) \\ - \frac{\sigma_{10}}{2} \cdot a^v \cdot Q_{vm}^* \cdot \frac{a^v}{v} & (v \neq 0) \end{cases}, & Q_v^{\#} &\equiv \begin{cases} \frac{\sigma_{10}}{4} \cdot (a^2 - g^2) \cdot \log \left(\frac{a^2}{\alpha} \right) & (v=0) \\ - \frac{\sigma_{10}}{2} \cdot (a^{2v+2} - g^{2v+2}) \cdot \frac{a^v}{2v+2} \cdot \frac{a^v}{v} & (v \neq 0) \end{cases}, \\ S_{vm}^{\#} &\equiv J_v \left(\frac{\kappa \cdot \beta_{vm} \cdot a}{a-g} \right), \end{aligned}$$

$$f_v(t) \equiv \begin{cases} \frac{\mu_0}{2\pi} I(t) \log\left(\frac{d}{\gamma}\right) & (v=0) \\ -\frac{\mu_0}{2\pi} I(t) a^v \cdot \frac{d^{-v}}{v} & (v \neq 0) \end{cases}$$

where d is distance between the center of the cylinder and the filament current, σ is the conductivity of the cylinder material, μ_0 is the permeability of the vacuum, α and γ are arbitrary positive constant values greater than a and d , respectively, and $I(t)$ is the preprogrammed waveform of the external filament current (A). α and γ appear on the introduction of the boundary condition to the integrated form of Eq. (2.9).

The new vector variable $x_v(t) \in \mathbf{R}^{(\lambda+1) \times 1}$ is defined as

$$x_v(t) = t(C_{v1}(t), C_{v2}(t), C_{v3}(t), \dots, C_{v\lambda}(t), D_v(t)).$$

Then, Eqs. (A.1) and (A.2), i.e. the v -sets of the $(\lambda+1)$ simultaneous first-order differential equations, are converted to v -sets of the vector differential equations. The initial condition can be set as

$$x_v(0) = t(0, 0, 0, \dots, 0, -f_v(0)).$$

The calculation with larger values of v and λ gives a more precise solution from an analytical point of view, but, conversely, too large a dimension of λ may deteriorate the accuracy of the solution from a numerical point of view. By substituting the solution of Eqs. (A.2) and (A.3) for $C_{v\lambda}(t)$ and $D_v(t)$ in Eq. (A.1), the vector potential in the conductor is obtained. Accordingly, the vector potential inside and outside the cylinder are given as follows;

$$A_z(\rho, \theta, t) = \sum_{v=0}^{\infty} h_v(\rho, t) \cos v\theta + \sum_{v=0}^{\infty} \sum_{\lambda=1}^{\infty} \frac{dC_{v\lambda}}{dt} \xi_{v\lambda}(\rho) \cos v\theta + \sum_{v=0}^{\infty} \frac{dD_v}{dt} \zeta_v(\rho) \cos v\theta$$

$$h_v(\rho, t) \equiv \begin{cases} -\frac{\mu_0}{2\pi} I(t) \log\left(\frac{d}{\gamma}\right) & (v=0) \\ \frac{\mu_0}{2\pi} I(t) \rho^v \cdot \frac{d^{-v}}{v} & (v \neq 0) \end{cases}$$

inside the cylinder:

$$\xi_{v\lambda}(\rho) \equiv \begin{cases} \frac{\sigma_1 \mu_0}{2} \int_g^a r J_v\left(\frac{\kappa \beta v_2 r}{a-g}\right) \log\left(\frac{r^2}{\alpha}\right) dr & (v=0) \\ -\frac{\sigma_1 \mu_0}{2} \cdot \frac{\rho^v}{v} \int_g^a r^{1-v} J_v\left(\frac{\kappa \beta v_2 r}{a-g}\right) dr & (v \neq 0) \end{cases}$$

$$\zeta_{v(\rho)} \equiv \begin{cases} \frac{\sigma_{10}}{2} \left[a^2 \log(a) - g^2 \log(g) - \frac{a^2 - g^2}{2} (1 + \log(\alpha)) \right] & (v=0) \\ -\frac{\sigma_{10}}{2} \cdot \frac{\rho^v \cdot a^2 - g^2}{v \cdot a^v} & (v \neq 0) \end{cases}$$

outside the cylinder:

$$\xi_{v\lambda}(\rho) \equiv \begin{cases} \frac{\sigma_{10}}{2} \cdot Q_{v\lambda}^* \cdot \log\left(\frac{\rho^2}{\alpha}\right) & (v=0) \\ -\frac{\sigma_{10}}{2} \cdot a^v \cdot Q_{v\lambda}^* \cdot \frac{\rho^{-v}}{v} & (v \neq 0) \end{cases}$$

$$\zeta_{v(\rho)} \equiv \begin{cases} \frac{\sigma_{10}}{4} \cdot (a^2 - g^2) \log\left(\frac{\rho^2}{\alpha}\right) & (v=0) \\ -\frac{\sigma_{10}}{2} \cdot (a^{2v+2} - g^{2v+2}) \cdot \frac{a^{-v}}{2v+2} \cdot \frac{\rho^{-v}}{v} & (v \neq 0) \end{cases}$$

The magnetic field is then calculated by the relation $\mathbf{B} = \text{rot} \mathbf{A}$. ■

III.2 Formulation of Coil-Vessel-Plasma Electromagnetic Interactions in a Tokamak for the Finite Element Analysis

1. Introduction

In the previous section it is understood that a point model of a plasma has difficulty to take volume effects into account. To provide against such a problem, an overall model of plasma equilibrium control shall be built up in this section. The most general method to deal with a time-variant numerical system is a finite element method, where several basic partial differential equations (PDEs) are simultaneously solved in integral formulas on the discretized finite meshes. The tokamak system can be expressed as only electromagnetic interactions to the exclusion of particle/energy transport in a plasma and neutral gas inside the vessel. Particle/energy transport phenomena in electromagnetic interactions still contains many open questions. However, fortunately, the following two quantities related to particle/energy transport play an important role in plasma equilibrium control; plasma pressure and conductivity profiles in a plasma column. These quantities could be determined if the transport phenomena are completely elucidated. For this moment, they are supposed to be artificially given as conditional waveforms. This will reproduce shape-variant rigid-body motion of a plasma resulting from electromagnetic interactions; as the time constants of particle/energy transport are much longer compared with that of electromagnetic interactions (except in the period that plasma is drastically evolving, such as current building-up or disruptions), a plasma equilibrium control system easily follows the change of plasma equilibrium quantities coming from the particle/energy transport. Therefore, the system design of plasma equilibrium control can be conducted without strict consideration of the transport phenomena. Analyses in the periods of current building-up, heating, pellet fueling, disruption, etc., may require strict involvement of the transport.

Electromagnetic interactions in a tokamak should be, strictly speaking, dealt in the 3-dimensional analytical space. To reduce the computational time for practical use, the 2-dimensional axisymmetric analysis is adopted. In that arise several problems: How to deal with a poloidal field (PF) coil composed of several turns connecting 3-dimensionally with each other? How to allow the voltage input of the PF coil power supply? How to deal with axisymmetric current flow in 2-dimensional space? How to express the boundary conditions? The answers to these questions will be discussed in the following sections.

In Section 2, the equations of the coil-vessel-plasma electromagnetic interactions are derived from basic Maxwell equations and a gauge equation. In Section 3, boundary conditions are classified. In Section 4, discretization of PDEs for numerical computation are presented and how to involve the boundary conditions in the analysis is discussed. In Section 5, the major numerical techniques peculiar to this analysis are presented: the method of automatic mesh generation and the handling method for large scale matrices.

2. PDE Formulation of the Coil-Vessel-Plasma Electromagnetic Interactions

The coil-vessel-plasma electromagnetic interactions in a tokamak plasma equilibrium can be regarded as those among static and dynamic conductors, where eddy current effects play an essential role. Displacement current is neglected hereafter in the discussion, but the electric field produced by surface charges are taken into account. The static Maxwell's equations, then, show the relation of the current density (\mathbf{j}) and magnetic flux intensity (\mathbf{B});

$$\begin{aligned} \operatorname{rot} \left(\frac{1}{\mu} \mathbf{B} \right) &= \mathbf{j} \\ \operatorname{div} \mathbf{B} &= 0, \end{aligned} \quad (2.1)$$

where μ is permeability. By introducing the vector potential \mathbf{A} ($\mathbf{B} = \operatorname{rot} \mathbf{A}$) from Eq. (2.2), Eq. (2.1) can be rewritten:

$$\operatorname{rot} \left(\frac{1}{\mu} \operatorname{rot} \mathbf{A} \right) = \mathbf{j} \quad (2.3)$$

Ohm's law shows the macroscopic relation of the current density (\mathbf{j}) and electric field (\mathbf{E});

$$\mathbf{j} = \sigma \cdot (\mathbf{E}_{\text{stop}} + \mathbf{E}_{\text{move}}) \quad (2.4)$$

where σ is a conductivity tensor. The electric field (\mathbf{E}_{stop}) is induced even if an object is standing at the same location and it can be expressed by using the vector and scalar potentials (\mathbf{A} and ϕ);

$$\mathbf{E}_{\text{stop}} = - \partial \mathbf{A} / \partial t - \operatorname{grad} \phi. \quad (2.5)$$

If an object is moving with the velocity of \mathbf{v} through the magnetic field \mathbf{B} , the other electric field (\mathbf{E}_{move}) is produced in the object according to

$$\mathbf{E}_{\text{move}} = \mathbf{v} \times \mathbf{B} = \mathbf{v} \times \operatorname{rot} \mathbf{A} \quad (2.6)$$

Consequently, Eqs. (2.3) through (2.6) yield the equation of \mathbf{A} and ϕ :

$$\text{rot} \left(\frac{1}{\mu} \text{rot} \mathbf{A} \right) = \sigma \cdot \left[\left(-\frac{\partial \mathbf{A}}{\partial t} - \text{grad} \phi \right) + \mathbf{v} \times \text{rot} \mathbf{A} \right] \quad (2.7)$$

One more equation is needed to solve \mathbf{A} and ϕ independently. The Coulomb gauge is adopted for the analysis:

$$\text{div} \mathbf{A} = 0 \quad (2.8)$$

These equations are presented in general forms. Hereafter the symbols of \mathbf{A} , \mathbf{B} and ϕ denote the total vector potential, magnetic field and scalar potential, respectively. Now we apply them to the following regions in a tokamak geometry.

- (a) The vacuum region.
- (b) The static conductor region (in the vacuum vessel and support structures).
- (c) The static forced current region.
- (d) The PF coil region.
- (e) The moving conductor region (in a plasma).

These regions are shown in Fig. 2.1.

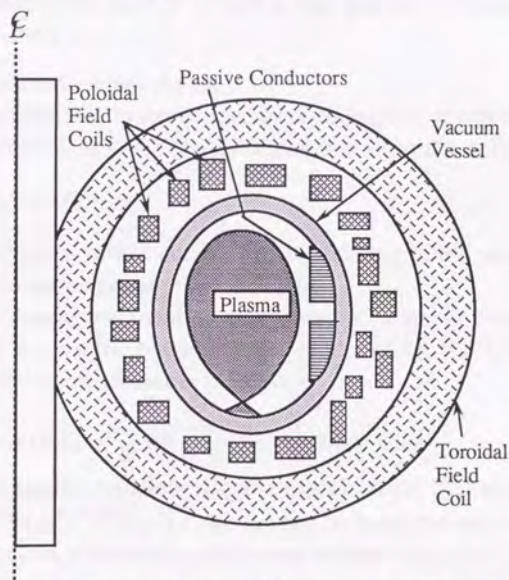


Fig. 2.1 Concept of Structural Components in a Tokamak

2.1 PDEs in the Vacuum, Static Conductors and Forced Current Regions

- (a) The vacuum region

No current flows in the vacuum region: $\mathbf{j}=0$ in Eq. (2.3), then:

$$\text{rot}\left(\frac{1}{\mu_0}\text{rot } \mathbf{A}\right) = \mathbf{0} \quad (2.9)$$

No charge exists in the vacuum region, either. The divergence of Eq. (2.5) vanishes. By using the gauge of $\text{div } \mathbf{A}=0$, then the scalar potential ϕ satisfies:

$$\Delta \phi = 0. \quad (2.10)$$

(b) The static conductor region (in the vacuum vessel and support structures)

As the object does not move, $\mathbf{v}=\mathbf{0}$ in Eq. (2.7).

$$\text{rot}\left(\frac{1}{\mu_0}\text{rot } \mathbf{A}_s\right) = \mathbf{j}_s = \sigma \cdot \left(-\frac{\partial \mathbf{A}}{\partial t} - \text{grad}\phi\right), \quad (2.11)$$

where \mathbf{j}_s is the current density flowing in the region of concern and \mathbf{A}_s is the vector potential produced by \mathbf{j}_s . As the conductors are not magnetic materials, the permeability is regarded to be the same with that in the vacuum ($\mu=\mu_0$). If the vacuum vessel with bellows has an anisotropic conductivity (σ is a tensor), electric charges may appear on the joint surface of the conductors having different conductivities. Except in such a case, $\text{grad}\phi$ in the right hand side of Eq. (2.11) vanishes.

(c) The static forced current region

If the current flowing in the conductor is completely controlled by a power supply, the current density is forcibly determined to be the desired value.

$$\text{rot}\left(\frac{1}{\mu_0}\text{rot } \mathbf{A}_F\right) = \mathbf{j}_F \quad (2.12)$$

where \mathbf{j}_F is the given forced current density flowing in the region of concern and \mathbf{A}_F is the vector potential produced by \mathbf{j}_F .

If the coils can be regarded as axisymmetric filament coils, the toroidal component of the vector potential, A_ω , produced by the forced current is given by the well-known formula as follows:

$$A_\omega(R, Z) = \frac{\mu_0 I}{4\pi} \left[\frac{4}{k} \sqrt{\frac{R_C}{R}} \left(\left(1 - \frac{k^2}{2}\right) K(k) - E(k) \right) \right], \quad (2.13)$$

where K and E are the complete elliptic integrals of the first and second kinds, $k^2 \equiv 4R_C \cdot R / \{(R_C + R)^2 + (Z_C - Z)^2\}$, (R_C, Z_C) and (R, Z) are the coil location and the observation point in cylindrical coordinates, respectively, I (A) is the filament coil current.

2.2 PDE in the Poloidal Field Coil Region

A PF coil is composed of several circular turns of copper conductor. To simplify the discussion, the following possible approximations are adopted:

- (i) The turn-to-turn connections are neglected. The PF coils are regarded to be axisymmetric.
- (ii) The current flows uniformly across the poloidal cross-sections of PF coils.
- (iii) The vector potential is uniform on the poloidal cross sections and the scalar potential is neglected because no charge is produced in the ideal axisymmetric geometry.
- (iv) The power supply is a perfect voltage source with negligibly small internal resistance.

On the contrary, the PF coil should keep two conditions;

- (#i) the total currents flowing across the poloidal cross sections of all turns belonging to a PF coil are all the same and
- (#ii) the voltage between the both ends of a PF coil is equal to that produced by the power supply.

Then the approximations and conditions result in the following equation:

$$\text{rot}\left(\frac{1}{\mu_0}\text{rot } \mathbf{A}_{\alpha\beta}\right) = \mathbf{j}_{\alpha\beta} = \frac{1}{\eta_{\alpha} S_{\alpha\beta}} \left[\mathbf{V}_{\alpha(t)} + 2\pi \sum_{\gamma} r_{\alpha\gamma} \left(-\frac{\partial \mathbf{A}_{\alpha\gamma}}{\partial t} \right) \right], \quad (2.14)$$

where $\mathbf{A}_{\alpha\gamma}$ is the vector potential on the γ -th turn of the α PF coil, $\mathbf{V}_{\alpha(t)}$ is the time-variant voltage vector produced by the power supply, the vectors of $\mathbf{A}_{\alpha\gamma}$ and $\mathbf{V}_{\alpha(t)}$ have only a toroidal component, $S_{\alpha\beta}$ and $r_{\alpha\beta}$ are the cross section and the major radius of the β -th turn of the α PF coil, respectively, η_{α} is the resistance of the α PF coil; $\eta_{\alpha} \equiv \Sigma 2\pi r_{\alpha\beta} / (\sigma \cdot S_{\alpha\beta})$.

2.3 PDE in the Moving Conductor Region (in a Plasma)

A plasma is presumed to be a kind of a zero-inertia conductor, that is moving axisymmetrically. Then Eq. (2.7) becomes:

$$\text{rot}\left(\frac{1}{\mu_0}\text{rot } \mathbf{A}_p\right) = \mathbf{j}_p = \sigma_p \left[\left(-\frac{\partial \mathbf{A}}{\partial t} - \text{grad}\phi \right) + \mathbf{v}_p \times \mathbf{B} \right], \quad (2.15)$$

where \mathbf{j}_p is the current density flowing in the region of concern, \mathbf{A}_p is the vector potential produced by \mathbf{j}_p , σ_p is the plasma conductivity tensor, \mathbf{v}_p is the plasma velocity. \mathbf{B} can be written as $\mathbf{B} = \mathbf{B}_{\text{FEM}} + \mathbf{B}_T$, where \mathbf{B}_{FEM} is the time-variant magnetic vector resulting from the finite element analysis and \mathbf{B}_T is the (time-invariant) toroidal field. A plasma is, strictly speaking, a magnetic medium, but the extent of its magnetization is negligibly small:

$$|\mu(\text{plasma}) - \mu_0| / \mu_0 \sim 0.001,$$

then the permeability is set μ_0 . The plasma pressure p , current density \mathbf{j}_p and magnetic field \mathbf{B} are connected by the equilibrium condition:

$$m_p d\mathbf{v}_p/dt = \text{grad } p - \mathbf{j}_p \times \mathbf{B} = \mathbf{0}, \quad (2.16)$$

where the inertia of a plasma is assumed to be zero and m_p is the negligibly small mass of a plasma.

Two problems arise in the analysis of these equations: (i) How to compose the conductivity tensor σ_p ? (ii) How to obtain the plasma velocity \mathbf{v}_p ? Now we consider Eq. (2.16) quantitatively to discuss the problem (i). In a high β plasma of JT-60 Upgrade, for example, the absolute values of p , \mathbf{j}_p and \mathbf{B} are as follows:

$$|\text{grad } p| \sim 10^3 \text{ N/m}^3 \text{ (in steep case)}, |\mathbf{j}_p| \sim 10^6 \text{ A/m}^2, |\mathbf{B}| \sim 4 \text{ N/(m}\cdot\text{A)}.$$

Then the angle of intersection of \mathbf{j}_p and \mathbf{B} , $\sin^{-1}[|\text{grad } p|/(|\mathbf{j}_p| \cdot |\mathbf{B}|)]$, is less than 0.02 degrees. This implies that the current \mathbf{j}_p can be regarded to flow approximately along the magnetic field \mathbf{B} . It is assumed that the \mathbf{B} -parallel component of \mathbf{E} induces $|\mathbf{j}_p|$ and that the scalar conductivity σ_p along \mathbf{B} is given as a preset condition in this formulation. The time constants of the \mathbf{j}_p equilibration and change of pressure are longer than several tens of milliseconds. In the aspect of numerical computation, if the time interval of discretized simulation is short enough, \mathbf{B} calculated in the previous time step, \mathbf{B}^{prev} , can be used to determine $|\mathbf{j}_p|$:

$$\begin{aligned} |\mathbf{j}_p| &= \sigma_p \frac{\mathbf{B}^{\text{prev}}}{|\mathbf{B}^{\text{prev}}|} \left[\left(-\frac{\partial A}{\partial t} - \text{grad}\phi \right) + \mathbf{v}_p \times \mathbf{B} \right], \\ &\approx \sigma_p \frac{\mathbf{B}^{\text{prev}}}{|\mathbf{B}^{\text{prev}}|} \left(-\frac{\partial A}{\partial t} - \text{grad}\phi \right), \end{aligned} \quad (2.17)$$

where $\mathbf{B}^{\text{prev}} \cdot (\mathbf{v}_p \times \mathbf{B}) = 0$, because $\mathbf{B}^{\text{prev}} \approx \mathbf{B}$. Then, by using Eq. (2.16), \mathbf{j}_p is determined according to Eq. (2.16):

$$\mathbf{j}_p \approx \sigma_p \left[\frac{\mathbf{B}^{\text{prev}}}{|\mathbf{B}^{\text{prev}}|^2} \left(-\frac{\partial A}{\partial t} - \text{grad}\phi \right) \right] \cdot \mathbf{B}^{\text{prev}} + \frac{\mathbf{B}^{\text{prev}} \times \text{grad } p}{|\mathbf{B}^{\text{prev}}|^2}, \quad (2.18)$$

where \mathbf{B} is approximated by \mathbf{B}^{prev} to avoid nonlinear formulation, and σ_p and $\text{grad } p$ are presumed to be the given time-variant functions of position.

Plasma motion shall be next considered from a macroscopic view point. Naturally plasma moving velocity is microscopically determined according to the force balance of Eq. (2.16) at each point in a plasma. As the PF coils, however, are designed to produce uniform magnetic field, all parts of a plasma column move at approximately the same speed with each other. Then, a plasma

is assumed to move like a zero-inertia rigid body. The velocity \mathbf{v}_p in the problem (ii) is determined by the macroscopic balance of force. Then the volume integral of Eq. (2.16) holds in a plasma conductor:

$$\int_{\Omega_p} (\mathbf{j}_p \times \mathbf{B} - \text{grad } p) dV = \int_{\Omega_p} \mathbf{j}_p \times \mathbf{B} dV = 0 \quad (2.19)$$

where Ω_p is the entire volume of a plasma, the volume integral of $\text{grad } p$ vanishes, because the pressure on the plasma surface is regarded to be zero; $\int \text{grad } p dV = \int p dS = 0$. The total magnetic field can be expressed as

$$\mathbf{B} = \text{rot } \mathbf{A}_s + \text{rot } \mathbf{A}_p + \text{rot } \mathbf{A}_{PF} + \mathbf{B}_T (+ \text{rot } \mathbf{A}_F). \quad (2.20)$$

In particular, the current flowing in the static conductors, \mathbf{j}_s , producing the magnetic field, $\text{rot } \mathbf{A}_s$, is divided into two parts: One is induced by the plasma motion and it is approximately proportional to \mathbf{v}_p in the Inconel vessel case (the scalar conductivity of Inconel #625 is $7.69 \times 10^5 \Omega^{-1} \text{m}^{-1}$), as is discussed in Chapter III.1. The other is induced by other couplings with the PF coils and static conductors themselves.

Axisymmetric motion is presumed to be currently considered. As only poloidal field is related to \mathbf{v}_p , the 2-dimensional magnetic field on the poloidal cross-section, $[\text{rot } \mathbf{A}_s](\mathbf{r}, \mathbf{v}_p)$, is calculated according to:

$$[\text{rot } \mathbf{A}_s](\mathbf{r}, \mathbf{v}_p) \approx \frac{\mu_0}{4\pi} \left[\int_{\Omega_v} \frac{[(\sigma(\mathbf{s}) \cdot \mathbf{F}(\mathbf{s})) \# (\mathbf{r} - \mathbf{s})] dV(\mathbf{s})}{|\mathbf{r} - \mathbf{s}|^3} \right] \cdot \mathbf{v}_p \quad (2.21)$$

where \mathbf{r} is the positional vector in cylindrical coordinates, $\mathbf{r} \equiv (R, Z)$, $\int dV(\mathbf{s})$ is the volume integral with respect to the positional vector \mathbf{s} , Ω_v is the entire volume of the static conductors,

$$\mathbf{F}(\mathbf{r}) \equiv - \frac{\mu_0}{4\pi} \int_{\Omega_p} \left\langle \frac{\partial (\mathbf{j}_p(\mathbf{s}))}{\partial \mathbf{s}} \middle| \frac{\partial}{\partial \mathbf{s}} \left(\frac{1}{|\mathbf{r} - \mathbf{s}|} \right) \right\rangle dV(\mathbf{s}) \quad (2.22)$$

and the definitions of $\langle \rangle$ and $[\#]$ are as follows:

$$\left\langle \frac{\partial (\mathbf{j}_p(\mathbf{s}))}{\partial \mathbf{s}} \middle| \frac{\partial}{\partial \mathbf{s}} \left(\frac{1}{|\mathbf{r} - \mathbf{s}|} \right) \right\rangle \equiv \left[\frac{\partial (\mathbf{j}_p(\mathbf{s}))}{\partial R} \middle| \frac{\partial}{\partial R} \left(\frac{1}{|\mathbf{r} - \mathbf{s}|} \right) \right] \in \mathbf{R}^{3 \times 2} \quad (2.23)$$

$$[\mathbf{M} \# \mathbf{u}] \equiv \left[\begin{pmatrix} \mathbf{m}_\alpha \\ \mathbf{m}_\beta \\ \mathbf{m}_\gamma \end{pmatrix} \# \begin{pmatrix} u_\alpha \\ u_\beta \\ u_\gamma \end{pmatrix} \right] \equiv \begin{bmatrix} \mathbf{m}_\beta \cdot \mathbf{u}_\gamma - \mathbf{m}_\gamma \cdot \mathbf{u}_\beta \\ \mathbf{m}_\gamma \cdot \mathbf{u}_\alpha - \mathbf{m}_\alpha \cdot \mathbf{u}_\gamma \\ \mathbf{m}_\alpha \cdot \mathbf{u}_\beta - \mathbf{m}_\beta \cdot \mathbf{u}_\alpha \end{bmatrix} \in \mathbf{R}^{3 \times 2} \quad (2.24)$$

where $\mathbf{M} \in \mathbf{R}^{3 \times 2}$, $\mathbf{m}_i \in \mathbf{R}^{3 \times 1}$ and $\mathbf{u}_i \in \mathbf{R}^{3 \times 1}$. By substitution of Eqs. (2.20) and (2.21) for Eq. (2.19), the macroscopic velocity \mathbf{v}_p is explicitly obtained.

In time evolution analysis, the velocity in the previous time step, $\mathbf{v}_p^{\text{prev}}$, has produced the eddy current in the static conductors, when the velocity \mathbf{v}_p at the current time step is being calculated. In addition, the current density flowing in the conductors, \mathbf{j}_s , cannot be decomposed into one induced by the plasma motion and the other. This implies that \mathbf{v}_p is not derived separately from $\mathbf{v}_p^{\text{prev}}$. Therefore, the magnetic field $\text{rot } \mathbf{A}_s$ produced by \mathbf{j}_s is conceptually divided into 2 components; $\text{rot } \mathbf{A}_s = [\text{rot } \mathbf{A}_s](\mathbf{v}_p^{\text{prev}}) + [\text{rot } \mathbf{A}_s](\text{others})$. The magnetic field induced by $\mathbf{v}_p^{\text{prev}}$ is given by the analysis in the static conductor region. Then $\mathbf{v}_p^{\text{calc}}$, that is obtained from Eqs. (2.19)–(2.21) at every time step, is based on the background field of $[\text{rot } \mathbf{A}_s](\mathbf{v}_p^{\text{prev}}) + [\text{rot } \mathbf{A}_s](\text{others})$. Consequently actual plasma velocity \mathbf{v}_p is given by the vector combination; $\mathbf{v}_p = \mathbf{v}_p^{\text{prev}} + \mathbf{v}_p^{\text{calc}}$. At the next time step, $\mathbf{v}_p^{\text{prev}}$ is replaced by newly obtained \mathbf{v}_p .

3. Boundary Conditions

The vacuum vessel having the toroidally non-uniform electrical conductivity shows the axis-asymmetric PF-coil field penetration, as is discussed in Chapter III.1. Three-dimensional analysis is required for the problem of concern. On the other hand, 3-dimensional analysis for the full tokamak geometry needs too many finite elements and too long computation time. "A right sectorial cylinder" is now chosen as a necessary minimum region for the analysis, because the tokamak is approximately composed of 4 to 12 divisions of the same sectorial components. In a case of n divisions, the interior angle of the sector, $\theta = 2\pi/n$ in the right sectorial cylinder. This right sectorial cylinder is bounded by 5 surfaces: two planes perpendicular ω -axis, S_{A+} and S_{A-} , two planes of the sector cut-ends perpendicular to Z -axis, S_{B+} and S_{B-} , and a curved surface, S_c ($R = (\text{a constant})$), as shown in Fig. 3.1. Now boundary conditions on the surfaces shall be specified: "B&E-periodic boundary condition" is applied on S_{A+} and S_{A-} , interfacing with each other. "B-parallel boundary conditions" are applied on S_{B+} , S_{B-} and S_c .

"The B&E periodic condition" is defined that the magnetic and electric field vectors on S_{A+} and S_{A-} are restricted to be the same at every period of the angle θ , with respect to the each normal vector on the planes. This can be written as the vector forms in the sectorial cylinder;

$$|\mathbf{B}| \text{ (on } S_{A+}) = |\mathbf{B}| \text{ (on } S_{A-}), \quad (3.1)$$

$$\mathbf{B} \cdot \mathbf{n} \text{ (on } S_{A+}) = \mathbf{B} \cdot \mathbf{n} \text{ (on } S_{A-}), \quad (3.2)$$

$$[\mathbf{B} \times \mathbf{n} \text{ (on } S_{A+})}]_Z = [\mathbf{B} \times \mathbf{n} \text{ (on } S_{A-})}]_Z, \quad (3.3)$$

$$|\mathbf{E}| \text{ (on } S_{A+}) = |\mathbf{E}| \text{ (on } S_{A-}), \quad (3.4)$$

$$\mathbf{E} \cdot \mathbf{n} \text{ (on } S_{A+}) = \mathbf{E} \cdot \mathbf{n} \text{ (on } S_{A-}), \quad (3.5)$$

$$[\mathbf{E} \times \mathbf{n} \text{ (on } S_{A+})}]_Z = [\mathbf{E} \times \mathbf{n} \text{ (on } S_{A-})}]_Z, \quad (3.6)$$

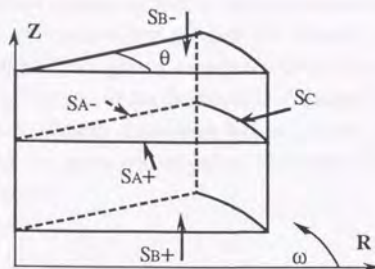


Fig. 3.1 The Analytical Boundary for a Tokamak Geometry Analysis (Surfaces of a Right Sectorial Cylinder)

where \mathbf{n} denotes the normal vector to the plane S_{A+} or S_{A-} , $[\mathbf{a}]_Z$ is the z -component of the vector \mathbf{a} , and $|\mathbf{a}|$ is the absolute value of the vector \mathbf{a} .

"The \mathbf{B} -parallel boundary condition" is defined that the magnetic field is parallel to the boundary planes, S_{B+} , S_{B-} and S_c , i.e.:

$$\mathbf{B} \cdot \mathbf{n} \text{ (on } S_{B+}, S_{B-} \text{ or } S_c) = 0. \quad (3.7)$$

This condition is a kind of approximation. Then the boundary planes having the \mathbf{B} -parallel condition are extended sufficiently far away from the main analytical region, so that such improper boundary conditions would not cause an unfavorable influence on the analysis.

Furthermore, if the analytical region has an up-and-down symmetry, " \mathbf{B} -perpendicular boundary condition" should be employed to save computer resources (memory and time). This condition is applied on the "midplane" (a mirror surface plane for the symmetry, that is often the equatorial plane of a torus), where the magnetic field line intersects perpendicularly to the midplane:

$$\mathbf{B} \times \mathbf{n} \text{ (on the midplane)} = \mathbf{0}. \quad (3.8)$$

Even if the PF coils are up-and-down symmetrically located, this condition cannot always be applied, because a plasma can move in the vertical directions up-and-down asymmetrically to the midplane.

These boundary conditions are utilized to reduce the number of unknown variables of the vector and scalar potentials at the nodes in the finite element

method. The way to impose the conditional equations on the discretized PDEs will be discussed in the following section.

4. Integral Formulation and Discretization

To apply the derived equations to the finite element analysis, discretization processes of the PDEs of concern are needed. Of several methods proposed for doing this, the method of weighted residuals is adopted. It is because the integral calculation is known to be numerically stable, and because energy principle for a tokamak system dynamics has not been found. The vector or scalar potential is used for a weight function. Now the PDEs to be discretized are summarized as follows:

(a) The vacuum region:

$$\operatorname{rot}\left(\frac{1}{\mu_0}\operatorname{rot}\mathbf{A}\right) = \mathbf{0} \quad (4.1)$$

(b) The static conductor region:

$$\operatorname{rot}\left(\frac{1}{\mu_0}\operatorname{rot}\mathbf{A}_s\right) = \sigma\left(-\frac{\partial\mathbf{A}}{\partial t} - \operatorname{grad}\phi\right) \quad (4.2)$$

(c) The static forced current region:

$$\operatorname{rot}\left(\frac{1}{\mu_0}\operatorname{rot}\mathbf{A}_F\right) = \mathbf{j}_F \quad (4.3)$$

(d) The PF coil region:

$$\operatorname{rot}\left(\frac{1}{\mu_0}\operatorname{rot}\mathbf{A}_{\alpha\beta}\right) = \frac{1}{\eta_{\alpha}\mathcal{S}_{\alpha\beta}}\left[\mathbf{V}_{\alpha}(t) + 2\pi\sum_{\gamma}r_{\alpha\gamma}\left(-\frac{\partial\mathbf{A}_{\alpha\gamma}}{\partial t}\right)\right] \quad (4.4)$$

(e) The moving conductor (plasma) region:

$$\operatorname{rot}\left(\frac{1}{\mu_0}\operatorname{rot}\mathbf{A}_P\right) = \sigma_P(t)\left[\frac{\mathbf{B}^{\text{prev}}}{(\mathbf{B}^{\text{prev}})^2}\left(-\frac{\partial\mathbf{A}}{\partial t} - \operatorname{grad}\phi\right)\right]\cdot\mathbf{B}^{\text{prev}} + \frac{\mathbf{B}^{\text{prev}}\times\operatorname{grad}p(t)}{(\mathbf{B}^{\text{prev}})^2} \quad (4.5)$$

The velocity of plasma motion is separately determined by Eq. (2.18). Finally, the above PDEs have commonly the same formula. Each PDE in each analytical region is solved simultaneously together with the Coulomb gauge condition:

$$\operatorname{rot}\left(\frac{1}{\mu_0}\operatorname{rot}\mathbf{A}\right) = \sigma\left(-\frac{\partial\mathbf{A}}{\partial t} - \operatorname{grad}\phi\right) + \mathbf{g}(t) \quad (4.6)$$

$$\operatorname{div}\mathbf{A} = 0, \quad (4.7)$$

where $\mathbf{g}(t)$ is a vector variable that is manipulated according to a control method.

Now the vector and scalar potentials, \mathbf{A} and ϕ , are used as the weight functions for Eqs. (4.6) and (4.7), respectively. After the multiplications, the volume integrals over the whole region Ω (of which the boundary is $\partial\Omega$) is performed. Then Eqs. (4.6) and (4.7) become:

$$\int_{\Omega} \left[\frac{1}{\mu_0} (\text{rot } \mathbf{A})^2 + \mathbf{A} \cdot \sigma \cdot \left(\frac{\partial \mathbf{A}}{\partial t} + \text{grad } \phi \right) - \mathbf{A} \cdot \mathbf{g}(t) \right] dV = \int_{\partial\Omega} \mathbf{A} \cdot \left(\frac{1}{\mu_0} \text{rot } \mathbf{A} \times \mathbf{n} \right) dS, \quad (4.8)$$

$$\int_{\Omega} \phi \cdot \text{div } \mathbf{A} dV = 0 \quad (4.9)$$

The discretization of Eqs. (4.8) and (4.9) on the meshes gives the basic finite element formulation. By imposing the boundary conditions, the solution is obtained as linear matrix calculations.

4.1 Discretization in Space and Time

The integral calculation is performed over discretized space and time. The 3-dimensional space is discretized into the finite number of elements. A type of the element adopted for this analysis is a 6-faced polyhedron (hexahedron) with 8 nodes. The vector and scalar potentials are defined at every node. An isoparametric linear function is used for interpolation inside the element. Figure 4.1 shows a hexahedral element in Descartes coordinates.

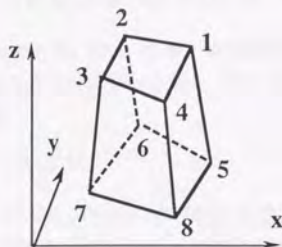


Fig. 4.1 The Hexahedral Element and Incidence Numbers

The definitions are as follows: The i -th vertex of the hexahedral element is (x_i, y_i, z_i) , $i=1-8$, in Descartes coordinates, as shown in Fig. 4.1. The vector and scalar potentials at the i -th vertex are similarly defined as (A_{xi}, A_{yi}, A_{zi}) and ϕ_i , $i=1-8$. Now the interpolation function for the potentials are defined using the parameters, ξ , η and ζ , $-1 \leq \xi, \eta$ or $\zeta \leq 1$: an arbitrary point (x, y, z) inside the hexahedron in Descartes coordinates is expressed by:

$$x = \sum_{i=1}^8 N_i(\xi, \eta, \zeta) \cdot x_i, \quad y = \sum_{i=1}^8 N_i(\xi, \eta, \zeta) \cdot y_i, \quad z = \sum_{i=1}^8 N_i(\xi, \eta, \zeta) \cdot z_i, \quad (4.10)$$

where $N_i(\xi, \eta, \zeta)$ is the interpolation function or "shape function" for the isoparametric linear element, defined as:

$$N_i(\xi, \eta, \zeta) \equiv \frac{1}{8} (1 + \xi_i \xi) (1 + \eta_i \eta) (1 + \zeta_i \zeta), \quad (4.11)$$

where $[[\xi_i, \eta_i, \zeta_i], i=1 \rightarrow 8] \equiv [(1,1,1), (-1,1,1), (-1,-1,1), (1,-1,1), (1,1,-1), (-1,1,-1), (-1,-1,-1), (1,-1,-1)]$.

The vector and scalar potentials at the point (x, y, z) are interpolated using the parameters (ξ, η, ζ) corresponding to (x, y, z) as follows:

$$A_x = \sum_{i=1}^8 N_i(\xi, \eta, \zeta) \cdot A_{x_i}, \quad A_y = \sum_{i=1}^8 N_i(\xi, \eta, \zeta) \cdot A_{y_i}, \quad A_z = \sum_{i=1}^8 N_i(\xi, \eta, \zeta) \cdot A_{z_i},$$

$$\phi = \sum_{i=1}^8 N_i(\xi, \eta, \zeta) \cdot \phi_i \quad (4.12)$$

Time is discretized using the parameter θ ($0 \leq \theta \leq 1$) according to the following simple expression:

$$t = (1 - \theta) t_n + \theta t_{n+1}, \quad (4.13)$$

where t_n denotes the time at the n -th time step. Other quantities are similarly time-discretized like:

$$A = (1 - \theta) \cdot A_n + \theta \cdot A_{n+1} \quad \text{or} \quad \phi = (1 - \theta) \cdot \phi_n + \theta \cdot \phi_{n+1}. \quad (4.14)$$

As the integral with respect to time is not needed in the solution of concern, the parameter θ is set a constant value 0.5. The time derivative is defined as the difference with time:

$$\partial A / \partial t = (A_{n+1} - A_n) / \Delta t, \quad (4.15)$$

where Δt is the interval of the discretized time step.

The derivations of the volume/surface integral calculations of Eqs. (4.8) and (4.9) are presented in detail in Appendix. Finally, Eqs. (4.8) and (4.9) are converted to the equations using the vectors which is composed of the vector and scalar potentials and the manipulated variables defined at the nodes:

$$\alpha_n \cdot (U_n \cdot \alpha_n + V_n \cdot \beta_n + W_n \cdot \gamma_n) + U_{n+1} \cdot \alpha_{n+1} + V_{n+1} \cdot \beta_{n+1} + W_{n+1} \cdot \gamma_{n+1} = 0, \quad (4.16)$$

$$\beta_n \cdot (S_n \cdot \alpha_n + S_{n+1} \cdot \alpha_{n+1}) = 0, \quad (4.17)$$

where

$$\alpha_n \equiv [A_{x_{n1}}, A_{y_{n1}}, A_{z_{n1}}; \dots, A_{x_{n18}}, A_{y_{n18}}, A_{z_{n18}}; -; A_{x_{nm8}}, A_{y_{nm8}}, A_{z_{nm8}}] \in \mathbf{R}^{3 \cdot 8 \cdot m \times 1},$$

$\beta_n \equiv [\phi_{n11}; \dots, \phi_{n18}; \dots; \phi_{nm1}; \dots, \phi_{nm8}] \in \mathbf{R}^{8 \cdot m \times 1}$,

$\gamma_n \equiv [g^{x_{n11}}, g^{y_{n11}}, g^{z_{n11}}; \dots, g^{x_{n18}}, g^{y_{n18}}, g^{z_{n18}}; \dots; g^{x_{nm8}}, g^{y_{nm8}}, g^{z_{nm8}}] \in \mathbf{R}^{3 \cdot 8 \cdot m \times 1}$,

m ; the number of the elements,

n ; the time step number,

A_{nij}^q ; the q -components of the vector potential at the j -th vertex in the i -th element at the n -th time step,

ϕ_{nij} ; the scalar potential at the j -th vertex in the i -th element at the n -th time step,

g_{nij}^q ; the q -components of the manipulated vector variable at the j -th vertex in the i -th element at the n -th time step,

$U_n (\in \mathbf{R}^{3 \cdot 8 \cdot m \times 3 \cdot 8 \cdot m})$, $V_n (\in \mathbf{R}^{3 \cdot 8 \cdot m \times 8 \cdot m})$, $W_n (\in \mathbf{R}^{3 \cdot 8 \cdot m \times 3 \cdot 8 \cdot m})$ and $S_n (\in \mathbf{R}^{3 \cdot 8 \cdot m \times 3 \cdot 8 \cdot m})$

; the coefficient matrices as a result of the integral calculation.

Eqs. (4.16) and (4.17) yields:

$$\begin{bmatrix} U_n & V_n \\ S_n & 0 \end{bmatrix} \cdot \begin{pmatrix} \alpha_n \\ \beta_n \end{pmatrix} + \begin{bmatrix} U_{n+1} & V_{n+1} \\ S_{n+1} & 0 \end{bmatrix} \cdot \begin{pmatrix} \alpha_{n+1} \\ \beta_{n+1} \end{pmatrix} + \begin{bmatrix} W_n \\ 0 \end{bmatrix} \cdot \gamma_n + \begin{bmatrix} W_{n+1} \\ 0 \end{bmatrix} \cdot \gamma_{n+1} = 0 \quad (4.18)$$

The unknown vector at the $(n+1)$ -th time step is given according to the following recurrence formula:

$$\begin{pmatrix} \alpha_{n+1} \\ \beta_{n+1} \end{pmatrix} = - \begin{bmatrix} U_{n+1} & V_{n+1} \\ S_{n+1} & 0 \end{bmatrix}^{-1} \cdot \left(\begin{bmatrix} U_n & V_n \\ S_n & 0 \end{bmatrix} \cdot \begin{pmatrix} \alpha_n \\ \beta_n \end{pmatrix} + \begin{bmatrix} W_n \\ 0 \end{bmatrix} \cdot \gamma_n + \begin{bmatrix} W_{n+1} \\ 0 \end{bmatrix} \cdot \gamma_{n+1} \right) \quad (4.19)$$

4.2 Shape Evolution

Plasma cross-sectional shape is evolving during discharge as a result of plasma movement induced by the change of fields and/or plasma internal quantities. This effect shall be involved in the finite element analysis.

A method to adapt grids to the moving object has been reported^[1], but this may require complicated algorithms and additional computation time between the time steps. Now is proposed the simpler method to adapt only the conductivities for the elements appropriately.

- (1) At first in every time step, the plasma shape is determined according to the algorithm, presented in Chapter II.
- (2) Then if an element having plasma conductivity in the previous time step is reassigned to vacuum along with the plasma movement, the conductivity is also reassigned to 0, and vice versa.
- (3) The calculation is started with new conductivity assignment.

The remaining problem is how to determine the values of conductivity for elements and will be discussed later in Section 6.

4.3 Imposition of Boundary Conditions

Boundary conditions (BCs) decrease the number of unknown independent vector and scalar potentials by imposing constraints on Eq. (4.19). This is expected to remarkably reduce the computation time. As is mentioned in Section 3, three types of boundary conditions are considered in this analysis; (a) **B**&**E** periodic BC, (b) **B**-parallel BC and (c) **B**-perpendicular BC. To discuss these discretized formulas, several definitions and useful formulas shall be introduced.

$$\mathbf{C} \equiv \begin{pmatrix} x_1, x_2, \dots, x_8 \\ y_1, y_2, \dots, y_8 \\ z_1, z_2, \dots, z_8 \end{pmatrix} \in \mathbf{R}^{3 \times 8}, \quad (4.20)$$

$$\mathbf{V} \equiv \begin{pmatrix} Ax_1, Ax_2, \dots, Ax_8 \\ Ay_1, Ay_2, \dots, Ay_8 \\ Az_1, Az_2, \dots, Az_8 \end{pmatrix} \equiv \begin{pmatrix} v_x \\ v_y \\ v_z \end{pmatrix} \in \mathbf{R}^{3 \times 8}, \quad (4.21)$$

$$\mathbf{f} \equiv {}^t(\phi_1, \phi_2, \dots, \phi_8) \in \mathbf{R}^{8 \times 1}, \quad (4.22)$$

$$\mathbf{p}(\xi, \eta, \zeta) \equiv {}^t(N_1(\xi, \eta, \zeta), N_2(\xi, \eta, \zeta), \dots, N_8(\xi, \eta, \zeta)) \in \mathbf{R}^{8 \times 1}, \quad (4.23)$$

$$\mathbf{n} \equiv {}^t(n_x, n_y, n_z), \quad \mathbf{e}_x \equiv {}^t(1 \ 0 \ 0), \quad \mathbf{e}_y \equiv {}^t(0 \ 1 \ 0), \quad \mathbf{e}_z \equiv {}^t(0 \ 0 \ 1), \quad (4.24)$$

$$\mathbf{W}(\xi, \eta, \zeta) \equiv \left(\frac{\partial \mathbf{p}}{\partial \xi} : \frac{\partial \mathbf{p}}{\partial \eta} : \frac{\partial \mathbf{p}}{\partial \zeta} \right) \left[\mathbf{C} \cdot \left(\frac{\partial \mathbf{p}}{\partial \xi} : \frac{\partial \mathbf{p}}{\partial \eta} : \frac{\partial \mathbf{p}}{\partial \zeta} \right)^{-1} \right] \in \mathbf{R}^{8 \times 3}, \quad (4.25)$$

Using these definitions, the following useful expressions are obtained:

$$\begin{pmatrix} x \\ y \\ z \end{pmatrix} = \mathbf{C} \cdot \mathbf{p}(\xi, \eta, \zeta), \quad (4.26)$$

$$\mathbf{A} \equiv \begin{pmatrix} Ax(x, y, z) \\ Ay(x, y, z) \\ Az(x, y, z) \end{pmatrix} = \mathbf{V} \cdot \mathbf{p}(\xi, \eta, \zeta) = \mathbf{P}(\xi, \eta, \zeta) \cdot \mathbf{u}, \quad (4.27)$$

$$\phi = {}^t \mathbf{f} \cdot \mathbf{p}(\xi, \eta, \zeta), \quad (4.28)$$

$$\frac{\partial}{\partial s} \begin{pmatrix} \xi \\ \eta \\ \zeta \end{pmatrix} = \left[\mathbf{C} \cdot \left(\frac{\partial \mathbf{p}}{\partial \xi} : \frac{\partial \mathbf{p}}{\partial \eta} : \frac{\partial \mathbf{p}}{\partial \zeta} \right)^{-1} \right] \cdot \mathbf{e}_s, \quad s=x, y, z, \quad (4.29)$$

$$\frac{\partial}{\partial s} \begin{pmatrix} Ax \\ Ay \\ Az \end{pmatrix} = \mathbf{V} \cdot \mathbf{W} \cdot \mathbf{e}_s, \quad s=x, y, z, \quad (4.30) \quad \frac{\partial \phi}{\partial s} = \mathbf{f} \cdot \mathbf{W} \cdot \mathbf{e}_s, \quad s=x, y, z, \quad (4.31)$$

$$\text{grad } \phi = {}^t \mathbf{W}(\xi, \eta, \zeta) \cdot \mathbf{f}, \quad (4.32) \quad \text{div } \mathbf{A} = {}^t \mathbf{h} \cdot \mathbf{Q}(\xi, \eta, \zeta) \cdot \mathbf{u}, \quad (4.33)$$

$$\text{rot } \mathbf{A} = \begin{pmatrix} v_z \cdot \mathbf{W} \cdot \mathbf{e}_y - v_y \cdot \mathbf{W} \cdot \mathbf{e}_z \\ v_x \cdot \mathbf{W} \cdot \mathbf{e}_z - v_z \cdot \mathbf{W} \cdot \mathbf{e}_x \\ v_y \cdot \mathbf{W} \cdot \mathbf{e}_x - v_x \cdot \mathbf{W} \cdot \mathbf{e}_y \end{pmatrix} \equiv \mathbf{Y} \cdot \mathbf{Q}(\xi, \eta, \zeta) \cdot \mathbf{u} \quad (4.34)$$

where

$$\mathbf{u} \equiv (v_x \quad v_y \quad v_z) \in \mathbb{R}^{24 \times 1}, \quad \mathbf{h} \equiv ({}^t\mathbf{e}_x \quad {}^t\mathbf{e}_y \quad {}^t\mathbf{e}_z) \in \mathbb{R}^{9 \times 1},$$

$$\mathbf{P} \equiv \begin{pmatrix} {}^t\mathbf{p} & \mathbf{0} & \mathbf{0} \\ \mathbf{0} & {}^t\mathbf{p} & \mathbf{0} \\ \mathbf{0} & \mathbf{0} & {}^t\mathbf{p} \end{pmatrix} \in \mathbb{R}^{3 \times 24},$$

$$\mathbf{Y} \equiv \begin{pmatrix} \mathbf{0} & -{}^t\mathbf{e}_z & {}^t\mathbf{e}_y \\ {}^t\mathbf{e}_z & \mathbf{0} & -{}^t\mathbf{e}_x \\ -{}^t\mathbf{e}_y & {}^t\mathbf{e}_x & \mathbf{0} \end{pmatrix} \in \mathbb{R}^{3 \times 9}, \quad \mathbf{Q} \equiv \begin{pmatrix} {}^t\mathbf{W} & \mathbf{0} & \mathbf{0} \\ \mathbf{0} & {}^t\mathbf{W} & \mathbf{0} \\ \mathbf{0} & \mathbf{0} & {}^t\mathbf{W} \end{pmatrix} \in \mathbb{R}^{9 \times 24}.$$

(a) **B&E**-periodic boundary condition

This condition is expressed by the vector forms of Eqs. (3.1)–(3.6) in the case shown in Fig. 3.1. It can be written as;

$$\mathbf{B} \text{ (on } S_{A-}) = \begin{pmatrix} \cos \theta & -\sin \theta & 0 \\ \sin \theta & \cos \theta & 0 \\ 0 & 0 & 1 \end{pmatrix} \cdot \mathbf{B} \text{ (on } S_{A+}) \equiv \mathbf{T} \cdot \mathbf{B} \text{ (on } S_{A+}) \quad (4.35)$$

$$\text{i.e., } \mathbf{Y} \cdot \mathbf{Q} \cdot \mathbf{u} \text{ (on } S_{A-}) = \mathbf{T} \cdot \mathbf{Y} \cdot \mathbf{Q} \cdot \mathbf{u} \text{ (on } S_{A+}). \quad (4.36)$$

Similarly the following relations are obtained:

$$\mathbf{A} \text{ (on } S_{A-}) = \mathbf{T} \cdot \mathbf{A} \text{ (on } S_{A+}). \quad (4.37)$$

$$\text{grad } \phi \text{ (on } S_{A-}) = \mathbf{T} \cdot \text{grad } \phi \text{ (on } S_{A+}). \quad (4.38)$$

(b) **B**-parallel boundary condition

This condition is expressed by the vector forms of Eq. (3.7); $\mathbf{B} \cdot \mathbf{n}$ (on S_{B+} , S_{B-} or S_C) = 0. It can be written as;

$$v_x \cdot (n_y \cdot \mathbf{W} \cdot \mathbf{e}_z - n_z \cdot \mathbf{W} \cdot \mathbf{e}_y) + v_y \cdot (n_z \cdot \mathbf{W} \cdot \mathbf{e}_x - n_x \cdot \mathbf{W} \cdot \mathbf{e}_z) + v_z \cdot (n_x \cdot \mathbf{W} \cdot \mathbf{e}_y - n_y \cdot \mathbf{W} \cdot \mathbf{e}_x) = 0. \quad (4.39)$$

(c) **B**-perpendicular boundary condition

This condition is expressed by the vector forms of Eq. (3.8); $\mathbf{B} \times \mathbf{n}$ (on the midplane) = 0. It can be written as;

$$\begin{pmatrix} v_z \cdot \mathbf{W} \cdot \mathbf{e}_y - v_y \cdot \mathbf{W} \cdot \mathbf{e}_z \\ v_x \cdot \mathbf{W} \cdot \mathbf{e}_z - v_z \cdot \mathbf{W} \cdot \mathbf{e}_x \\ v_y \cdot \mathbf{W} \cdot \mathbf{e}_x - v_x \cdot \mathbf{W} \cdot \mathbf{e}_y \end{pmatrix} = k \begin{pmatrix} n_x \\ n_y \\ n_z \end{pmatrix}, \quad (4.40)$$

where k is a proportional constant. The elimination of k in Eq. (4.40) yields 2 independent equations.

These conditional equations can be totally described in a formula;

$$\mathbf{M} \cdot \mathbf{q} = \mathbf{0}, \quad (4.41)$$

where \mathbf{q} is the $\mathbf{R}^{i \times 1}$ vector composed of all the related element of the vector and scalar potentials introduced in the boundary conditions, \mathbf{M} is the $\mathbf{R}^{j \times i}$ matrix whose elements are determined by the relations of Eqs. (4.36)–(4.40) and the integer j is greater than i . The method to reduce the unknown variables is now discussed. Eq. (4.41) can be rewritten as:

$$\mathbf{X} \cdot \mathbf{M} \cdot \mathbf{Z}^{-1} \cdot \mathbf{Z} \cdot \mathbf{q} = \mathbf{0}, \quad (4.42)$$

where \mathbf{Z} is the $\mathbf{R}^{i \times i}$ matrix to permute the rows of Eq. (4.41), \mathbf{X} is the $\mathbf{R}^{j \times j}$ matrix to transform $\mathbf{X} \cdot \mathbf{M} \cdot \mathbf{Z}^{-1}$ in the following way:

$$\mathbf{X} \cdot \mathbf{M} \cdot \mathbf{Z}^{-1} = [\mathbf{I} \quad \mathbf{N}], \quad (4.43)$$

where \mathbf{I} is the $\mathbf{R}^{j \times j}$ unit matrix and \mathbf{N} is the $\mathbf{R}^{j \times (i-j)}$ matrix. The vectors \mathbf{b}_1 and \mathbf{b}_2 are defined as;

$$\mathbf{Z} \cdot \mathbf{q} \equiv \begin{bmatrix} \mathbf{b}_1 \\ \mathbf{b}_2 \end{bmatrix}, \text{ i.e. } \mathbf{q} \equiv \mathbf{Z}^{-1} \cdot \begin{bmatrix} \mathbf{b}_1 \\ \mathbf{b}_2 \end{bmatrix}, \quad \mathbf{b}_1 \in \mathbf{R}^{j \times 1}, \quad \mathbf{b}_2 \in \mathbf{R}^{(i-j) \times 1}. \quad (4.44)$$

Using Eq. (4.44), Eq. (4.42) becomes

$$\mathbf{b}_1 + \mathbf{N} \cdot \mathbf{b}_2 = \mathbf{0}. \quad (4.45)$$

Finally, by the substitution of \mathbf{b}_1 in Eq. (4.45) for Eq. (4.44), the variable vector \mathbf{q} is expressed by only the independent vector \mathbf{b}_2 :

$$\mathbf{q} \equiv \mathbf{Z}^{-1} \cdot \begin{bmatrix} -\mathbf{N} \\ \mathbf{I} \end{bmatrix} \cdot \mathbf{b}_2. \quad (4.46)$$

Eq. (4.46) results in the reduction of the unknown variables \mathbf{b}_1 in the vector $[\alpha_n, \beta_n]$ in the Eq. (4.19).

5. Numerical Computation Techniques

The solution of Eq. (4.19) with Eq. (4.46) is understood to give the values of the vector and scalar potentials on the finite element vertices. In reality, however, the difficulties arise in this calculation. The major difficulties are as follows:

(a) The existing method to generate the finite meshes makes too much troubles, though the mesh design is not always so essential a task in the finite element analysis.

(b) The coefficient matrices are sparse ones with a large scale dimension. If all the elements of the matrices are kept in the computer memory, then huge amount of memory area is needed. However, this required memory may reach impractical size from the view point of the present computer technology.

To resolve these problems, an automatic mesh generator for a tokamak has newly developed, and the "position-tagged (PT) matrix" — a kind of the wave front method^[2] — is also proposed for the sparse matrix handling in the computer. The PT matrix is defined to hold only nonzero elements accompanied by their positions of (row, column) in the matrix. These results are discussed in this section.

5.1 Automatic 2-dimensional Mesh Generator for a Tokamak

A tokamak is often approximated to have an axisymmetric geometry. This is based on the fact that the plasma current distributions are regarded to be equal at any poloidal cross sections. It must be noted that plasma current flows helically in the toroidal plasma. An axisymmetric geometry is then assumed for a plasma and the PF coils in this analysis. The analytical region is the right sectorial cylinder, as discussed in Section 3. However, 2-dimensional mesh production is at first performed, and 3-dimensional meshes can be made by turning the 2-dimensional mesh on the central axis of a tokamak. Therefore, 2-dimensional mesh generator is a basic tool for the FEM analysis.

The components related to tokamak plasma equilibrium control on a poloidal cross section are shown in Fig. 2.1. They can be classified as;

(a) a plasma, (b) a vacuum vessel, (c) PF coils, (d) conductors and (e) a background vacuum. The features of these components and the methods to produce the meshes shall be explained below.

(i) A plasma and a background vacuum

As the area occupied by the plasma can not be specified beforehand, a fixed square with small cross section is simply chosen as the figure of elements inside the vacuum vessel. Another fixed square with the larger cross section is chosen as an element figure for a background vacuum. (This process is called the division of the "standard square mesh.")

This standard mesh is automatically generated by specifying only the sizes of square elements.

(ii) A vacuum vessel

A vacuum vessel figure usually looks like a belt string on the poloidal cross section. A vacuum vessel is divided into several layers of belt mesh. (This process is called the division of the "belt mesh.")

This standard mesh is automatically generated by (a) numerically defining the figure of the vacuum vessel, and (b) specifying the number of layers and that of division along the belt of vacuum vessel.

(iii) PF coils and conductors

A bundle of a PF coil is usually composed of several turns of coils. Each turn has a rectangle cross section and is insulated from other turns. This bundle is divided into meshes independently of the standard meshes is superposed on the vacuum. Conductors are also similarly divided into meshes. (This process is called the division of the "PF coil bundle mesh.")

This standard mesh is automatically generated by specifying the sizes and positions of the PF coil turns, conductors and insulators.

The meshes of the components divided by these processes must be linked with each other. Two types of linkage are now considered: (a) Linkage of the belt mesh with the standard mesh. (b) Linkage of the PF coil mesh with the standard mesh.

The simple algorithm is adopted for the linkage (a): Every node on the belt mesh is connected to the nearest node on the standard mesh inside and outside the vessel. However, the overlapped elements may be produced as a result of the connection process, as shown in Fig. 5.1. To provide against this, all connections are checked and if the intersection is detected, the second (or third,...) nearest node is selected as a linking node.

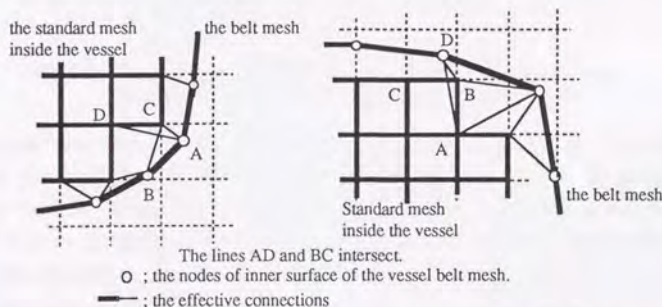


Fig. 5.1 The Examples of the Illegal Linkages between the Belt Mesh and Standard Mesh inside the Vacuum Vessel

The linkage (b) encounters a slight difficult problem: The clearance between a bundle of a PF coil and the vessel or another PF coil bundle is so narrow that no node on the standard mesh can be kept. For such a case, the following procedures are developed for the linkage.

- (i) The size of a PF coil bundle is reduced so that at least one element space be produced between the adjacent bundles. (see Fig. 5.2 (a) and (b))
- (ii) Every node on the reduced bundle is connected to the nearest node on the standard mesh. (see Fig. 5.2 (c))
- (iii) The PF coil bundle is enlarged to the real size with preserving the connections. (see Fig. 5.2 (d))

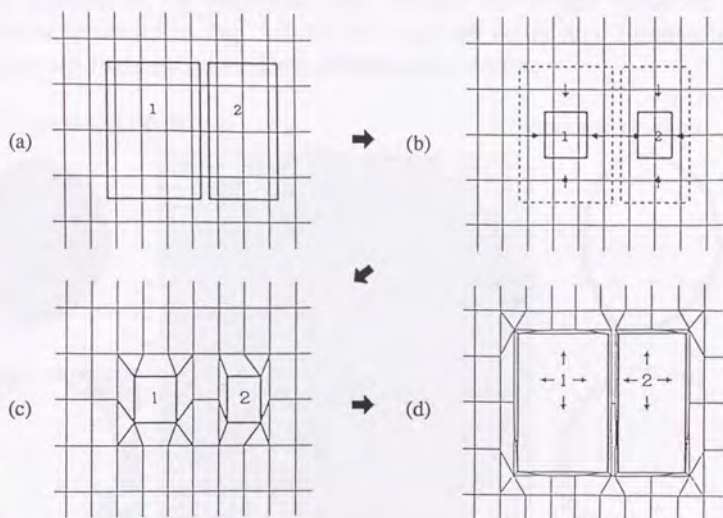


Fig. 5.2 The Procedure of Linking Nodes of the PF Coils Mesh and Those of the Standard Mesh outside the Vacuum Vessel

In case that too small elements for the vacuum be found, a method to decrease the number of the small elements is introduced. In advance a rectangle area is divided into larger square elements than the standard ones. Then this area is superposed on the rectangle area of standard mesh. The linkage algorithm is that every node on the rectangle superposed mesh is connected to the nearest node on the standard mesh. (This process is called the "superposition of the divided area.")

The procedures of the automatic mesh generator are summarized as follows:

- (1) The input data are specified; the sizes of standard square elements, the figure of the vacuum vessel, the number of layers and that of division along the belt, the sizes and positions of PF coil turns or conductors, etc.
- (2) After the vacuum vessel is located, the standard meshes are generated inside/outside the vessel. The linkage (a) process is performed.
- (3) The nodes on the standard meshes overlapped by the PF coil locations are removed. The linkage (b) process is performed.
- (4) If too small elements are found in the vacuum, superposition of the divided area is conducted.

As an example of the generated mesh division for JT-60U based on this algorithm is shown in Fig. 5.3. In this case, all nodes and 2-dimensional elements are produced on the same poloidal cross section.

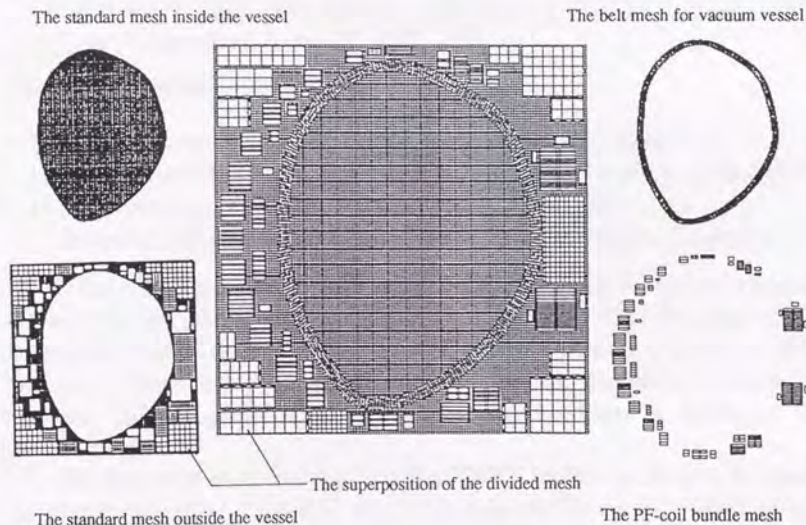


Fig. 5.3 Mesh Divisions in the JT-60U Case (All processes are separately shown.)

5.2 Position-tagged Matrix for Large Scale Linear Algebra

In the finite element analysis, the large number of elements are needed for precise calculation. To reduce the required computer memory, a matrix composed of only nonzero elements is naturally expected. This idea was first introduced in the reference [2]. Concept of a position-tagged (PT) matrix proposed for this analysis is now explained.

A sparse matrix $S \in R^{n \times n}$ is defined as

$S_{i, m(i,r)} \neq 0$, $i = 1, 2, \dots, n$, and $r=1, 2, \dots, q(i)$, and the other elements = 0,
where i and r ; the integers,

$S_{i, j}$; the i -th row and j -th column element of the matrix S ,

$m(i,r)$; the integer function denoting the column position of the r -th non-zero element in the i -th row ($m(i,r) \leq n$), and

$q(i)$; the integer function denoting the number of nonzero elements in the i -th row ($q(i) \leq n$).

This matrix can be converted to a reduced matrix without deterioration of information;

i -th row: $[q(i), \{m(i,r), r=1, 2, \dots, q(i)\}, \{S_{im(i,r)}, r=1, 2, \dots, q(i)\}]$, $i=1, 2, \dots, n$

This information is divided into the index and value parts;

i -th row index: $[q(i), \{m(i,r), r=1, 2, \dots, q(i)\}]$, $i=1, 2, \dots, n$

i -th row value: $[S_{im(i,r)}, r=1, 2, \dots, q(i)]$, $i=1, 2, \dots, n$

These are rewritten as the following 1-dimension arrays:

$[q(1), \{m(1,1), m(1,2), \dots, m(1,q(1))\}, q(2), \{m(2,1), m(2,2), \dots, m(2,q(2))\}, \dots$
 $\dots, q(n-1), \{m(n-1,1), m(n-1,2), \dots, m(n-1,q(n-1))\}, q(n), \{m(n,1), m(n,2), \dots, m(n,q(n))\}]$.
 $[S_{1m(1,1)}, S_{1m(1,2)}, \dots, S_{1m(1,q(1))}, S_{2m(2,1)}, S_{2m(2,2)}, \dots, S_{2m(2,q(2))}, \dots$
 $\dots, S_{(n-1)m(n-1,1)}, S_{(n-1)m(n-1,2)}, \dots, S_{(n-1)m(n-1,q(n-1))}, S_{nm(n,1)}, S_{nm(n,2)}, \dots, S_{nm(n,q(n))}]$.

As all the elements of the former array are integers, 2 bytes per an element are used for the matrix with less dimension than 32767. The elements of the latter array require floating point data with double precision (8 bytes for each element). These forms of the PT matrix minimize the utilized computer memory, while programs of the matrix linear algebra should be developed for the PT matrix.

The preconditioned conjugate gradient (PCG) method is adopted to obtain the matrix inversion. The PCG method is then rebuilt corresponding to the introduction of the PT matrix. The LU decomposition of the PT matrix is used for the preconditioning process. These calculation algorithms can be referred to the references^[3] for the finite element method.

5.3 Calculation Procedures of this Analysis

The calculation flow are summarized below:

- (i) The meshes are generated using the automatic mesh generator, introduced in Subsection 5.1.

- (ii) The material constants are set for all divided elements.
- (iii) The boundary conditions are set according to the algorithm introduced in Subsection 4.3.
- (iv) The initial state parameters, preset waveforms and other constants are prepared for the simulation.
- (v) The vector equations are composed according to the algorithm mentioned in Subsections 4.1 and 4.2, and are solved using the PT matrix algebra introduced in Subsection 5.2.
- (vi) Time step is advanced and the process (iv) is repeated till the expected time steps are completed.

6. Concluding Remarks

Formulation of coil-vessel-plasma electromagnetic interactions in a tokamak has been conducted and numerical methods have been developed for the finite element analysis. However, there still remains several problems to be discussed as follows:

In theoretical aspects:

- (a) The method to determine the conductivity tensor and pressure profile in a plasma has not yet been developed. Even without this, the analysis for the nominal plasma will be possible, because the control system design is required to know the plasma electromagnetic behavior at the current flat top. Hence, this analysis can give a precise model for investigation of plasma control algorithms with the realistic conductivity and pressure evolutions.
- (b) The conductivity tensor and pressure profile are results from microscopic transport analysis, while the plasma is macroscopically manipulated. How to reproduce the interactions between macro- and micro-phenomena is still left as a big problem.

In technical aspects:

- (a) It seems to take a lot of time to compose the vector equation and to compute the solution with the mesh division shown in Fig. 5.3. The faster computer with large memory is desired.

It is believed that the solution of these problems leads us to the more advanced understanding for tokamak plasma equilibrium control.

References in Chapter III.2

- [1] Flaherty, J.E., et al. (ed.) "Adaptive Methods for Partial Differential Equations," The Society for Industrial and Applied Mathematics (1989).
 - [2] Washizu, H., et al. (ed.) "Handbook of Finite Element Methods," p.73, Baifukan (Tokyo) 1981 (in Japanese).
 - [3] Hesteness, M.R. & Stiefel, E. "Methods of conjugate gradients for solving linear systems," Journal of Research of the National Bureau of Standards, Vol.49, (1952), pp.409-436.
- Reid, J.K., "On the method of conjugate gradients for the solution of large sparse systems of linear equations," Large Sparse Sets of Linear Equations (Reid, J.K. (ed.)), Academic Press (1971).
- Concus, P., et al., "A generalized conjugate gradient method for the numerical solution of elliptic partial differential equations," Sparse Matrix Computations (Bunch, J.R. & Rose, D. (ed.)), Academic Press (1976).

Appendix Discretization of the surface/volume integrals.

In this analysis, the vector equation is composed by discretization of the PDEs. The method of weighted residuals is adopted as the discretization method. Now the basic integral equation formulas are as follows:

$$\int_{\Omega} \left[\frac{1}{\mu_0} (\text{rot } \mathbf{A})^2 + \mathbf{A} \cdot \sigma \cdot \left(\frac{\partial \mathbf{A}}{\partial t} + \text{grad } \phi \right) - \mathbf{A} \cdot \mathbf{g}(t) \right] dV = \int_{\partial \Omega} \mathbf{A} \cdot \left(\frac{1}{\mu_0} \text{rot } \mathbf{A} \times \mathbf{n} \right) dS, \quad (\text{A.1})$$

$$\int_{\Omega} \phi \cdot \text{div } \mathbf{A} dV = 0 \quad (\text{A.2})$$

To make derivations easier, the vector definitions and useful expressions are again introduced in the same way as in Subsection 4.3.

$$\mathbf{C} \equiv \begin{pmatrix} x_1, x_2, \dots, x_8 \\ y_1, y_2, \dots, y_8 \\ z_1, z_2, \dots, z_8 \end{pmatrix} \in \mathbf{R}^{3 \times 8}, \quad (\text{A.3}) \quad \mathbf{V} \equiv \begin{pmatrix} Ax_1, Ax_2, \dots, Ax_8 \\ Ay_1, Ay_2, \dots, Ay_8 \\ Az_1, Az_2, \dots, Az_8 \end{pmatrix} \equiv \begin{pmatrix} v_x \\ v_y \\ v_z \end{pmatrix} \in \mathbf{R}^{3 \times 8}, \quad (\text{A.4})$$

$$\mathbf{f} \equiv {}^t(\phi_1, \phi_2, \dots, \phi_8) \in \mathbf{R}^{8 \times 1}, \quad (\text{A.5})$$

$$\mathbf{p}(\xi, \eta, \zeta) \equiv {}^t(N_1(\xi, \eta, \zeta), N_2(\xi, \eta, \zeta), \dots, N_8(\xi, \eta, \zeta)) \in \mathbf{R}^{8 \times 1}, \quad (\text{A.6})$$

$$\mathbf{n} \equiv {}^t(n_x, n_y, n_z), \quad \mathbf{e}_x \equiv {}^t(1 \ 0 \ 0), \quad \mathbf{e}_y \equiv {}^t(0 \ 1 \ 0), \quad \mathbf{e}_z \equiv {}^t(0 \ 0 \ 1), \quad (\text{A.7})$$

$$\mathbf{W}(\xi, \eta, \zeta) \equiv \left(\frac{\partial p}{\partial \xi} \ ; \ \frac{\partial p}{\partial \eta} \ ; \ \frac{\partial p}{\partial \zeta} \right) \cdot \left[\mathbf{C} \cdot \left(\frac{\partial p}{\partial \xi} \ ; \ \frac{\partial p}{\partial \eta} \ ; \ \frac{\partial p}{\partial \zeta} \right)^T \right]^{-1} \in \mathbf{R}^{8 \times 3}, \quad (\text{A.8})$$

$$\phi = {}^t \mathbf{f} \cdot \mathbf{p}(\xi, \eta, \zeta), \quad (\text{A.9}) \quad \text{grad } \phi = {}^t \mathbf{W}(\xi, \eta, \zeta) \cdot \mathbf{f}, \quad (\text{A.10})$$

$$\mathbf{A} = \mathbf{V} \cdot \mathbf{p}(\xi, \eta, \zeta) = \mathbf{P}(\xi, \eta, \zeta) \cdot \mathbf{u}, \quad (\text{A.11}) \quad \text{div } \mathbf{A} = {}^t \mathbf{h} \cdot \mathbf{Q}(\xi, \eta, \zeta) \cdot \mathbf{u}, \quad (\text{A.12})$$

$$\text{rot } \mathbf{A} = \begin{pmatrix} v_z \cdot \mathbf{W} \cdot \mathbf{e}_y - v_y \cdot \mathbf{W} \cdot \mathbf{e}_z \\ v_x \cdot \mathbf{W} \cdot \mathbf{e}_z - v_z \cdot \mathbf{W} \cdot \mathbf{e}_x \\ v_y \cdot \mathbf{W} \cdot \mathbf{e}_x - v_x \cdot \mathbf{W} \cdot \mathbf{e}_y \end{pmatrix} \equiv \mathbf{Y} \cdot \mathbf{Q}(\xi, \eta, \zeta) \cdot \mathbf{u}, \quad (\text{A.11})$$

where

$$\mathbf{u} \equiv {}^t(v_x \ v_y \ v_z) \in \mathbf{R}^{24 \times 1}, \quad \mathbf{h} \equiv {}^t({}^t \mathbf{e}_x \ {}^t \mathbf{e}_y \ {}^t \mathbf{e}_z) \in \mathbf{R}^{9 \times 1},$$

$$\mathbf{P} \equiv \begin{pmatrix} {}^t \mathbf{p} & \mathbf{0} & \mathbf{0} \\ \mathbf{0} & {}^t \mathbf{p} & \mathbf{0} \\ \mathbf{0} & \mathbf{0} & {}^t \mathbf{p} \end{pmatrix} \in \mathbf{R}^{3 \times 24},$$

$$\mathbf{Q} \equiv \begin{pmatrix} {}^t \mathbf{W} & \mathbf{0} & \mathbf{0} \\ \mathbf{0} & {}^t \mathbf{W} & \mathbf{0} \\ \mathbf{0} & \mathbf{0} & {}^t \mathbf{W} \end{pmatrix} \in \mathbf{R}^{9 \times 24}, \quad \mathbf{Y} \equiv \begin{pmatrix} \mathbf{0} & -{}^t \mathbf{e}_z & {}^t \mathbf{e}_y \\ {}^t \mathbf{e}_z & \mathbf{0} & -{}^t \mathbf{e}_x \\ -{}^t \mathbf{e}_y & {}^t \mathbf{e}_x & \mathbf{0} \end{pmatrix} \in \mathbf{R}^{3 \times 9}$$

The integral calculation in the volume of an element is performed with respect to the variables (ξ, η, ζ) , that are changed from variables (x, y, z) in Descartes coordinates. This aims at fixing the interval of volume integral as:

$$\int_{\Omega_E} \Pi(x,y,z) \cdot dV = \int_{-1}^{+1} \int_{-1}^{+1} \int_{-1}^{+1} \Pi(\xi,\eta,\zeta) \cdot \det \mathbf{J} \cdot d\xi d\eta d\zeta \quad (\text{A.12})$$

where Ω_E is the volume of an element, Π is the function for the integrand as shown in Eqs. (A.1) and (A.2), and $\det \mathbf{J}$ is the determinant of the Jacob matrix \mathbf{J} :

$$\mathbf{J}(\xi,\eta,\zeta) \equiv \mathbf{C} \cdot \begin{pmatrix} \frac{\partial \mathbf{p}}{\partial \xi} & \frac{\partial \mathbf{p}}{\partial \eta} & \frac{\partial \mathbf{p}}{\partial \zeta} \end{pmatrix} \in \mathbf{R}^{3 \times 3} \quad (\text{A.13})$$

Then the volume integrals for an element in the left hand side of Eq. (A.1) can be discretized as follows:

$$\int_{\Omega_E} (\text{rot } \mathbf{A})^2 \cdot dV = {}^t \mathbf{u} \cdot \left[\int_{-1}^{+1} \int_{-1}^{+1} \int_{-1}^{+1} {}^t \mathbf{Q} \cdot {}^t \mathbf{Y} \cdot \mathbf{Y} \cdot \mathbf{Q} \cdot \det \mathbf{J} \cdot d\xi d\eta d\zeta \right] \cdot \mathbf{u} \quad (\text{A.14})$$

$$\int_{\Omega_E} \mathbf{A} \cdot \boldsymbol{\sigma} \cdot \frac{\partial \mathbf{A}}{\partial t} \cdot dV = {}^t \mathbf{u} \cdot \left[\int_{-1}^{+1} \int_{-1}^{+1} \int_{-1}^{+1} {}^t \mathbf{P} \cdot \boldsymbol{\sigma} \cdot \mathbf{P} \cdot \det \mathbf{J} \cdot d\xi d\eta d\zeta \right] \cdot \frac{\partial \mathbf{u}}{\partial t} \quad (\text{A.15})$$

$$\int_{\Omega_E} \mathbf{A} \cdot \boldsymbol{\sigma} \cdot \text{grad } \phi \cdot dV = {}^t \mathbf{u} \cdot \left[\int_{-1}^{+1} \int_{-1}^{+1} \int_{-1}^{+1} {}^t \mathbf{P} \cdot \boldsymbol{\sigma} \cdot {}^t \mathbf{W} \cdot \det \mathbf{J} \cdot d\xi d\eta d\zeta \right] \cdot \mathbf{f} \quad (\text{A.16})$$

$$\int_{\Omega_E} \mathbf{A} \cdot \mathbf{g}(t) \cdot dV = {}^t \mathbf{u} \cdot \left[\int_{-1}^{+1} \int_{-1}^{+1} \int_{-1}^{+1} {}^t \mathbf{P} \cdot \mathbf{g}(t) \cdot \det \mathbf{J} \cdot d\xi d\eta d\zeta \right] \quad (\text{A.17})$$

The surface integral in the right hand side of Eq. (A.1) can be discretized as follows: (This integral is performed only in the boundary elements.)

$$\int_{\partial \Omega_E} \mathbf{A} \cdot (\text{rot } \mathbf{A} \times \mathbf{n}) \cdot dS = - {}^t \mathbf{u} \cdot \left[\int_{-1}^{+1} \int_{-1}^{+1} {}^t \mathbf{P} \cdot \mathbf{N} \cdot \mathbf{Y} \cdot \mathbf{Q} \cdot \det \mathbf{J} \cdot d\alpha \cdot d\beta (\gamma = \pm 1) \right] \cdot \mathbf{u} \quad (\text{A.18})$$

where \mathbf{N} is the matrix defined as:

$$\text{rot } \mathbf{A} \times \mathbf{n} = - \begin{pmatrix} 0 & -n_z & n_y \\ n_z & 0 & -n_x \\ -n_y & n_x & 0 \end{pmatrix} \cdot \text{rot } \mathbf{A} \equiv - \mathbf{N} \cdot \text{rot } \mathbf{A} \quad (\text{A.19})$$

(α, β, γ) are the permutations of (ξ, η, ζ), and Eq. (A.18) shows the integral over the surface defined by $\gamma = +1$ or -1 , as an example.

The volume integral in the left hand side of Eq. (A.2) can be discretized as follows:

$$\int_{\Omega E} \phi \cdot \text{div } \mathbf{A} \cdot dV = \int_{-1}^{+1} \int_{-1}^{+1} \int_{-1}^{+1} \mathbf{p} \cdot \mathbf{h} \cdot \mathbf{Q} \cdot \text{det } \mathbf{J} \cdot d\xi d\eta d\zeta \cdot \mathbf{u} \quad (\text{A.20})$$

The summation of Eqs. (A.14)–(A.20) for all elements with time discretization yields the vector formula of the concerned equations of Eqs. (4.16) and (4.17). ■

Chapter IV

Plasma Equilibrium Control Systems with Computers

JT-60 plasma control is performed by a supervisory controller, a measurement system and by actuators such as the poloidal/toroidal field coil power supplies, gas injectors, neutral beam injection (NBI) heating system, radio frequency (RF) heating system and pellet injectors. One of the most important characteristics of JT-60 is a fully digital control system.

After an eight-year design and construction period, the system started in operation in April 1985. During three years of operation, the system has been improved many times. In 1989, the plasma control system was composed of mini-computers, fast array processors and CAMAC modules.

From 1989 through 1991 April, JT-60 vacuum vessel and PF coil system is completely reconstructed to improve the plasma performance. As the plasma shape of JT-60 Upgrade (JT-60U) is highly elongated, the faster feedback control is required. Then hardware for plasma control system is superseded by the VME processors and input/output devices. The software is newly developed for more flexible and simple operation.

In this chapter, the specifications of the systems for JT-60 and JT-60U, including technological aspects of hardware and software, are presented. The actual real-time control functions are explained in detail and the results are also described. The emergency termination methods, which are indispensable for a large tokamak plant, are presented.

IV.1 The JT-60 Plasma Control System (1985~1989)

1. Introduction

Control system design often premises adequate understanding of the whole system. Unfortunately, for a tokamak plasma, such an understanding does not exist. However, if the plasma is to be generated and maintained for its investigation, a control system is needed. To accommodate this deficiency in understanding, the control system must have a structurally wide range of flexibility to tune the control methods. The flexibility has to be accompanied by the reliability. To satisfy the requirement above, we decided to build a digital control system composed of computers and standardised CAMAC equipment although the unavoidable dead-time of such a system possibly makes the control characteristics worse. The resolution is to set the sampling interval as short as possible. Therefore, high speed and accurate calculation are added as indispensable requirements.

In the software aspects, it is necessary to apply various control methods to the system. We prepared many alternative plasma control structures, which are easily changed by setting the discharge conditions, and ensured that an adequate number of signals were input to permit various types of calculations.

It is not, of course, possible to avoid all undesirable events, because we often make mistakes or hardware becomes broken. In order to provide against such unexpected events, several plasma termination methods were prepared for operational safety. Some are classified as prevention, and others are as treatment after an event.

Thus, "flexibility", "reliability", "high speed and accuracy" and "safety" are adopted as major principles for design of JT-60 plasma control system.

2. System Configuration

2.1 Changes of System Design Circumstances

At the first stage of design in 1979, JT-60 plasma real-time control aimed at equilibrium control (position and shape control) using only poloidal field (PF) coils. This control necessitates a feedback loop fast and precise enough to vary the position and shape according to their desired waveforms. Since the plasma evolves to the configuration determined by the external poloidal field at the Alfvén velocity, stabilization of the equilibrium depends on the curvature of the applied vertical magnetic field and on the eddy currents induced by movement of the plasma column. The JT-60 plasma, whose cross-section is

circular, is positionally stable even with an outside divertor. The PF coils are used control the plasma to follow preprogrammed waveforms of the equilibrium configuration, not to stabilize the position. For these purposes, a control cycle time of 1 msec was determined to be adequate. This cycle time was also a limitation of the computers available at that time. To realize the requirement, 16-bit fast mini-computers were selected as a supervisor and 16-bit fast micro-computers were arranged hierarchically below the supervisor to perform the parallel control and calculations for PF coil power supplies.

Stimulated by the addition of other control actuators, such as the heating systems and the gas injectors, the system design was reviewed in 1980. Initially, these additional actuators were planned to be controlled according to the preprogrammed waveforms, but safe operation of a high beta plasma was thought to necessitate careful control of both configuration and plasma particle transport. Since the supervisor of equilibrium control did not have the capability to do more calculations within the 1 msec, and the characteristic time constant of plasma particle transport is long enough to allow slower control, it was decided to add another class of control above the equilibrium controller with a 10 msec control cycle time to provide room for complicated logic and calculations. Thus the basic structure of plasma control system was designed to have two hierarchical feedback loops.

After the first plasma was obtained in April 1985, many improvements to the system were proposed as the experiments advanced. These necessitated more calculations to obtain the precise plasma parameters and to avoid damage to the PF and toroidal field (TF) coils. To solve this problem without making the system characteristics worse, we adopted two methods: pipeline processing and the addition of fast array processors. Then, the supervisor for equilibrium control was improved to be four-step-pipeline system with two fast array processors. The requirement of this system is "to obtain the desired plasma as safely as possible." This system being operated in 1985-1989 will be discussed in the following sections.

2.2 Outline of Data Flow

As mentioned before, the control system contains two feedback loops. The major loop is for plasma heating and gas fueling control, and the minor loop is for plasma equilibrium control which is executed by five sets of PF coils[*].

[*]: In JT-60, five sets of PF coils are prepared for the equilibrium control. Their controlled equilibrium parameters are below. Ohmic heating coil (OH-) coil vs. Ip. Vertical field (V-) coil vs. DR. Horizontal field (H-) coil vs. DZ. Quadrupole field (Q-) coil vs. D30. Outside Magnetic limiter (Divertor) (M-) coil vs. Dt. Strictly speaking, these correspondences are not perfect because of mutual interactions between the coils and parameters.

The plasma parameters are derived from the signals of electromagnetic detectors transferred from the measurement system.

The major loop supervisor (called the Real-Time Control Computer or RTCC) has the desired waveforms of plasma parameters and observes their actual quantities in real time. The commands for additional heating power and gas flow rate are transferred to the RF heating system and gas injectors, respectively. The commands to NBI heating system are sent as timing pulses after conversion from heating power to the appropriate number of units. The commands of the horizontal position (DR), vertical position (DZ), clearance between the wall and plasma surface (D30) and separatrix line route at the divertor throat (Dt) (as shown in Fig. 2.1) are transferred from the RTCC to the minor loop supervisor. The RTCC is kicked to execute the real-time program by a 10-msec-cycle clock.

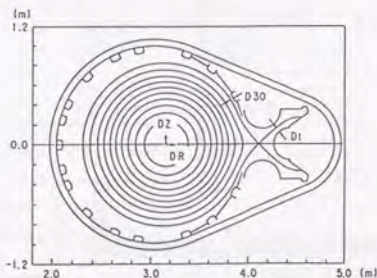


Fig. 2.1 JT-60 Cross Section and Equilibrium Parameters

The minor loop supervisor (the Feedback Control Computer or FBCC) controls the PF coil power supplies so as to track the plasma equilibrium parameters issued by the RTCC and transfers the commands of the coil current to the direct digital controllers (DDCs). In particular, the plasma current (I_p) is transferred to the OH-coil DDC through the FBCC from the RTCC. The FBCC is kicked to execute the real-time program by a 1-msec-cycle clock.

The DDCs control their thyristor firing angles to track the commands from the FBCC as fast as possible. A modern minimal-time control algorithm is applied to the calculations in the DDCs. The gas injector controller, which receives the gas flow-rate from the RTCC, simply outputs voltages to Piezo-electric valves corresponding to the commands. The RF heating system, which receives the injection power, phase and frequency from the RTCC, simply obeys the commands and informs the RTCC of the device status. The NBI heating system simply obeys the timing signal of ON/OFF from the RTCC and

informs the RTCC of the device status. The magnetic field intensity, the plasma current and one-turn voltage, which are measured by the electromagnetic detectors, are transferred to the RTCC and FBCC every 1 msec. The diagnostic system also transfers the data to the RTCC every 1 msec. The data flow is shown in Fig. 2.2.

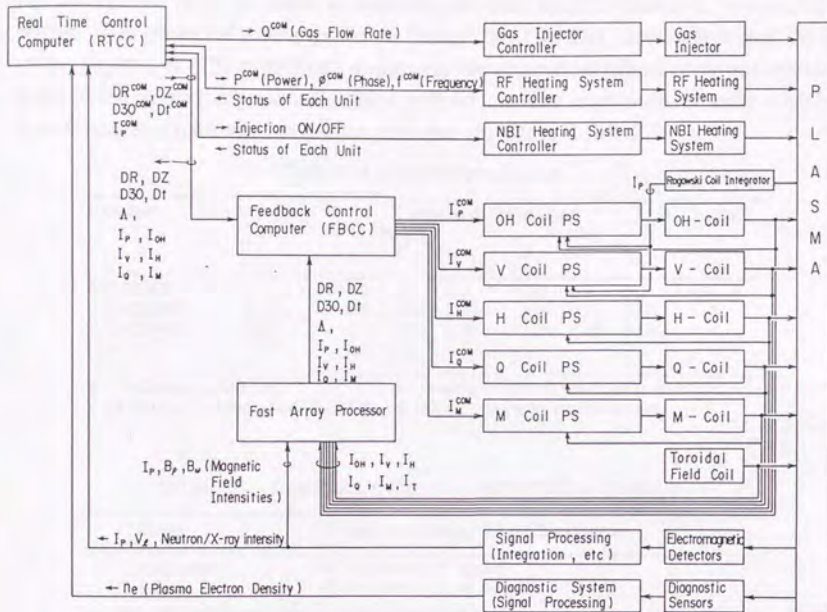


Fig. 2.2 Data Flow of Plasma Control System

2.3 Hardware Specification and Configuration

Since the specification and configuration of the chosen hardware decide the maximum performance of system, they were carefully designed. 16-bit mini-computers with a floating arithmetic processor ("HIDIC 80E" made by Hitachi Ltd.) were adopted for the RTCC and FBCC from the view point of calculation speed. As other controllers, 16-bit micro-computers ("i8086" made by Intel Co. Ltd. and "HIDIC-08L" made by Hitachi Ltd) were adopted; CAMAC auxiliary controller modules which contain i8086 or HIDIC-08L were developed by Toshiba Corp. and Hitachi Ltd. 16-bit array processors ("Zip 3216" made by Mercury Co., USA) were used for the pre-step to the FBCC. Their specifications are shown in Table 2.1.

As computer-device interfaces, CAMAC devices are assigned to be used in all control systems, because they are fast, reliable and easy to restore if broken. Communications between processors are also made through CAMAC highways; both byte serial and branch highways. CAMAC drivers which generate the byte serial mode and branch mode signals were newly developed for the HIDIC 80E. In order to increase the data transfer speed, a "command buffer" was prepared in the driver to "burst" the CAMAC commands and data to the highways. The command sequences are registered micro-program which is included in an assigned assembler instruction. The data transfer rates which a software and hardware overhead time are shown in Table 2.2.

Table 2.1 Computer Specification

Computer	Clock (Hz)	Calculation Speed (μ sec)						Note
		Integer			Floating			
		+	\times	+	+	\times	+	
HIDIC 80E	a	1.2	1.3	3.8	3.0	3.4	5.2	
ACM(i8086)	2.5M	6.5	36.0	36.0	42.0	31.0	35.0	b
ACM(H-08L)	13M	2.3	12.0	15.0	22.0	52.0	67.0	
Zip 3216	20M	0.1	0.1	-	-	-	-	c

a: Cycle time is 480 nsec.

b: Floating arithmetic processor is AMD5911A.

c: Arithmetic processor is AMD29116.

d: All the processors are 16-bit ones.

Table 2.2 Data Transfer Rate from HIDIC 80E to CAMAC

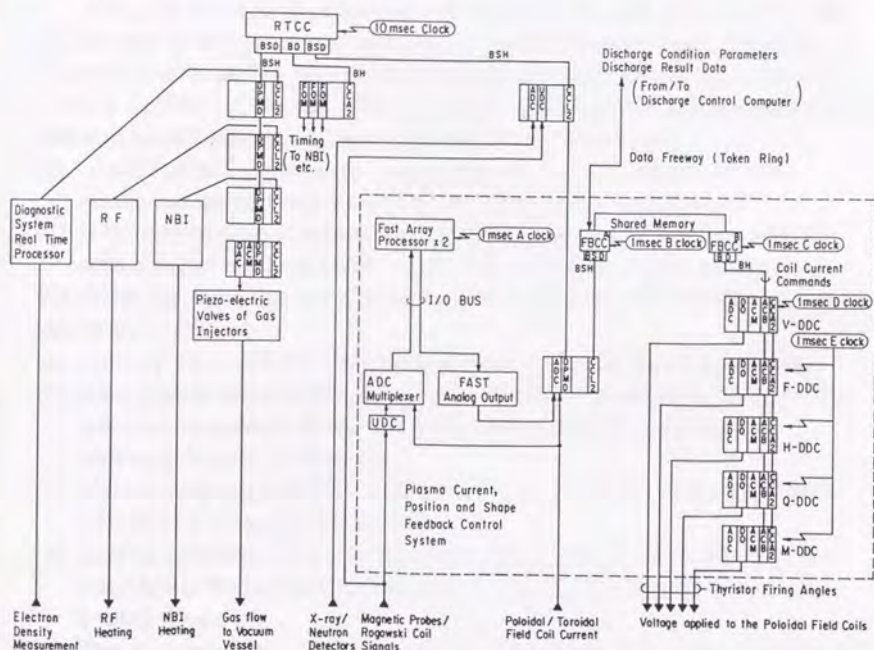
Driver	K words (commands) to L modules (crates)
Byte Serial	$80 + 2.8 \times K \times L$ (μ sec)
Branch	$77 + 3.6 \times K \times L$ (μ sec)

For the communications between processors, a mail box method is used. Two CAMAC modules were developed for this purpose. One is an auxiliary controller with branch highway port (ACB), which has a 24-bit register and can connect to the branch highway. The other is a dual port memory with CAMAC standard defined port (DPMD), which has a 128-word (1 word = 24 bits) memory and can connect to the byte serial highway. They are accessible to their data buffers from both the CAMAC dataway port and the highway port. They, therefore, make it possible for two processors to communicate quickly without interfering with each other.

Data handshakes ("synchronization") between processors are controlled by 1 msec/10 msec clocks. A clock pulse generator (CPG) counts a 16 MHz basic oscillation and generates 1 msec/10 msec clock with 50 % duty; a fan out module (FOM) distributes them to proper subsystems. The clock interrupts

each processor to execute its own real-time program. The time lag from the interrupt signal is 40 μ sec in the case of the HIDIC 80E. Five delayed clocks are used to perform the handshakes through five groups of pipeline processing. (A, B, C, D and E clocks shown in Fig.2.3). Each 1 msec clock is delayed by a timing pulse generator (TMG), with a digit of 10 μ sec.

When the RTCC transmits the timing pulse signal to the devices after the judgment of plasma states or the calculation of commands, it accessed the FOM from the CAMAC dataway and generates the signal. This is another usage of the FOM.



RTCC: Realtime control computer, FBCC^{A,B}: Feedback control computer, ACM: Auxiliary controller with micro-computer, ADC: Analog to digital converter, UDC: Up-down counter (digital integrator), DAC: Digital to analog converter, BD: Branch driver, BSD: Byte serial driver, CCL2: Type-L2 crate controller, CCA2: Type-A2 crate controller, BH: Branch highway, BSH: Byte serial highway, FOM: Fan out module that can generate the timing signals by CAMAC dataway functions, ACB: Auxiliary controller with BH ports, DO: Digital output, Fast Array Processor: Zip 3216 made by Mercury Co., DPMD: Dual port memory with CAMAC-defined port, ▲ :Inputs, ▼: Outputs.

Fig. 2.3 Plasma Control System Configuration

As the raw data from the magnetic sensors are differentiated signals of magnetic field intensity, and integration process is necessary. A digital

integration method was developed instead of usual analog integration: The voltage of the raw signal is converted to pulse chains with a frequency which is offset linear with the voltage, and then an up-down counter (UDC) integrates the pulses.

The hardware structure composed of the devices mentioned is shown in Fig. 2.3.

3. System Characteristics

3.1 Phase Control

Since the duration of JT-60 tokamak discharge is about 10 sec at most, the plasma state is always varying and there is strictly no steady state. However, it is convenient for design consideration that the discharge should be divided into a finite number of periods. These periods were selected corresponding to different control objectives. This has the following advantages.

- (1) In each period, different real-time programs can be performed. This means that unnecessary branching can be saved in the program.
- (2) If the plasma state is judged not to meet the objective of the next period, such a period can be skipped. This is one way to avoid a dangerous state.

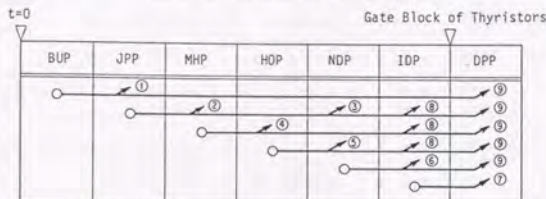
We divide the discharge into 7 periods, called "phases." The definitions of the phases are as follows:

- (a) Build up phase (BUP): The objective of this phase is plasma production.
- (b) Joule plasma phase (JPP): The plasma current is increased according to its reference waveform. At the end of this phase, the target plasma for additional heating is obtained.
- (c) Main heating phase (MHP): The plasma is increased in its beta value with additional heating by NBI and RF.
- (d) Heating off phase (HOP): In this phase and the next phase the plasma beta value has to be decreased. The kinetic energy is released with additional heating turned off.
- (e) Plasma density (n_e) down phase (NDP): In this phase, the kinetic energy is released with gas injection decreased. Lest the plasma reach the density limit in the next phase, the density has to be decreased sufficiently.
- (f) Plasma current (I_p) damping phase (IDP): finally, magnetic energy is released with OH-coil current decreased. Gate block sequences in the PF coil power supplies start after I_p becomes low enough.
- (g) Data processing phase (DPP): In this phase, plasma feedback control is completely abandoned, but data sampling is continued usually without a plasma.

Phases (d), (e) and (f) can be considered one continuous procedure for termination of discharge and are called "soft landing phases."

Phase control is managed by the RTCC. The RTCC shifts the phase when the plasma satisfies the shifting conditions or according to the schedule. This is shown in Table 3.1. The FBCC recognizes the current phase by interrupt signals from the RTCC. The FBCC changes the feedback gain matrices corresponding to the phases.

Table 3.1 Scheme of Phase Shift



- ①: if I_p control starts.
- ②: if n_e becomes enough high at the scheduled shift timing to MHP.
- ③: if OH-, V- or M-coil current beats the certain level.
if n_e becomes enough lower than the certain level. (prevention from runaway discharge.)
if I_p becomes bigger than the certain level.
if this phase period becomes longer than the allowable time.
if this soft landing sequence is triggered by the hardwired system. *1
- ④: if MHP period reaches the scheduled shift timing to HOP.
the same as ③.
- ⑤: if HOP period reaches the scheduled shift timing to NDP after heating devices completely stop.
- ⑥: if NDP period reaches the scheduled shift timing to IDP.
if D-stop *2 is interrupted.
- ⑦: if IDP period reaches the gate block timing, if I_p control starts.
if I_p is completely extinguished.
- ⑧: if D-stop *2 is interrupted.
- ⑨: if I_p is completely extinguished.
- ①→②→④→⑤→⑥→⑦: normal phase transitions.
- *1: Hardwired interlock system composed of metal wires and relay logics is also prepared for JT-60 protection.
- *2: D-stop is explained later in Section 6.
- *3: Conditions in judgment are usually given as discharge conditions.

3.2 Preprogrammed Control and Feedback Control

From a structural point of view, control methods can be classified, roughly speaking, into two groups: open loop and closed loop. In open loop control, a command is generated according to a preset schedule. This method does not modify the system characteristics, such as poles or zeroes of the transfer function, and thus cannot stabilize an unstable system. During a transient period, open loop control can provide the feature of feed-forward. In closed loop or feedback control, commands are generated according to an algorithm from observed data. This method modifies system dynamics so that

the system may become resistant against noises and fluctuations. In this control, the waveforms of basic reference parameters such as I_p and nominal values still have to be preprogrammed.

Table 3.2 Preprogrammed Waveform List

No.	Preprogrammed waveform	Sym.	Range	Precision ^a (1 digit =)	Pitch	Preset compl.	Note
1	Plasma current	I_p	0-3.5 MA	1.582 kA	10 ms	RTCC	
2	Major radius deviation	DR	-1-1 m	0.01 cm	10 ms	RTCC	
3	Vertical position deviation	DZ	-1-1 m	0.01 cm	10 ms	RTCC	
4	Plasma-wall clearance	D 30	0-1 m	0.01 cm	10 ms	RTCC	
5	Separatrix line-throat clearance	Dt	0-11 cm	0.01 cm	10 ms	RTCC	
6	Electron density	n_e	$0-5 \times 10^{14} \text{ cm}^{-3}$	$5 \times 10^9 \text{ cm}^{-3}$	10 ms	RTCC	Measured value is line-integrated
7	OH-coil voltage	V_{OH}	-2.5-0 kV	1 V	1 ms	OH-DDC	OH-Coil: 60 turns
8	H-coil current	I_H	-22-22 kA	12.89 A	1 ms	FBCC	
9	Q-coil current	I_Q	-15-35 kA	29.30 A	1 ms	FBCC	
10	Q-coil proportion coef.	α_Q	-0.1-0.1	0.0001	1 ms	FBCC	} alternative
11	M-coil current	I_M	0-120 kA	70.31 A	1 ms	FBCC	
12	M-coil proportion coef.	α_M	0-0.1	0.0001	1 ms	FBCC	} alternative
13	Gas flow rate	Q	0-200 Pa m ³ /sec	0.01 Pa m ³ /s	10 ms	RTCC	
14	NBI power	P_{NBI}	0-20 MW	1 kW	10 ms	RTCC	
15	RF power	P_{RF}	0-11 MW	11 kW	10 ms	RTCC	
16	RF phase	ϕ_{RF}	0-360 deg	5 deg	10 ms	RTCC	
17	RF frequency	f_{RF}	1.74-2.23 GHz	150 MHz	10 ms	RTCC	

^a As all waveform values are converted to 16-bit integers in the computer, dynamical range is -32768 ~ +32767 digits. This precision means not the control one, but the calculation one in the computer.

A preprogrammed waveform is divided into the groups defined by phases. When the phase is jumped over to another phase, the pointer of waveforms is also jumped to the top address of the corresponding phase. How to produce the preprogrammed waveforms in the computer has to be paid slight attention. As the scheduled waveform is possibly skipped, the simple skip of absolute value of waveform would create a discontinuity. Therefore, the waveform must be converted to a time-series of differentiated data prior to discharges. Supposing the raw waveforms is described as a time-series of

$$f(1), f(2), f(3), \dots, f(n),$$

then the converted time-series is

$$f(1), Df(2), Df(3), \dots, Df(n),$$

where $f(i)$ denotes the value at $t=i \cdot \Delta t$, and Δt is a sampling interval and $Df(i)=f(i)-f(i-1)$. The actual waveform is recomposed in real time by

$$g(i+1) = g(i) + Df(j),$$

where $g(i)$ is the recomposed value at $t=i\Delta t$, $g(0)=0$, $g(1)=f(1)$ and j indicates the position of the waveform pointer ($j=i+1$, if on schedule). This method can produce continuous commands even in the case of a phase skip. The gas flow-rate is an exception. As this is originally the differential value in respect to the plasma density, further differentiation is not necessary. Thus, the absolute value of the gas injection flow-rate must be produced even if the phase is skipped. Table 3.2 shows the preprogrammed waveform list with range, precision, preset computer, etc.

Feedback control is performed on I_p , plasma electron density (n_e) and plasma configuration (DR, DZ, D30 and Dt). The RTCC generates and transfers I_p to the OH-DDC through the FBCC. I_p is controlled by the OH-DDC according to conventional proportional control with a voltage limiter shown in Fig. 3.1(a), because plasma inductance and electrical resistance are so changeable that the minimal-time control gain can not be fixed.

The density (n_e) has to be well controlled especially in additional heating experiments, because effective heating requires appropriate density. It is controlled by the RTCC according to a proportional control algorithm with a limiter; a preprogrammed waveform of gas flow-rate is still used for the nominal value, shown in Fig. 3.1(b).

The FBCC compares DR, DZ, D30 and Dt transferred from the RTCC with the corresponding values calculated from the observed signals. The deviation derived from a proportional and differential (PD) algorithm is added to the nominal values which can be chosen from the coil current sampled every 1 msec or the preprogrammed waveform. Thus the FBCC algorithm can be described as

$$\mathbf{I}^{\text{command}}(k) = \mathbf{I}^{\text{command}}(k) + \mathbf{I}^{\text{deviation}}(k)$$

$$\mathbf{I}^{\text{deviation}}(k) \equiv \mathbf{G} \cdot \{\mathbf{Dy}(k) + \mathbf{H} \cdot (\mathbf{Dy}(k) - \mathbf{Dy}(k-1))\} \cdot I_p$$

where \mathbf{I} is a coil current vector ($=^t(I_v, I_H, I_Q, I_M)$),
 \mathbf{G} and \mathbf{H} are $R^{4 \times 4}$ gain matrices, $\mathbf{Dy}(k) = \mathbf{y}^{\text{command}}(k) - \mathbf{y}^{\text{observed}}(k)$,
 k denotes the discrete representation of time, and
 \mathbf{y} is a state vector ($=^t(\text{DR}, \text{DZ}, \text{D30}, \text{Dt})$).

The gain matrices are constant during each phase. It would be preferable to give the gain matrices as waveforms, but it was impossible with the available computer memory. The DDCs for V, H, Q and M coils receive the commands of coil currents, and convert these to the firing angles of thyristors which determine the voltage applied to the coils. A minimal-time control algorithm is applied to this conversion process. The gains are calculated with inductances and electrical resistances of coils. The block diagram is shown in Fig. 3.1(c).

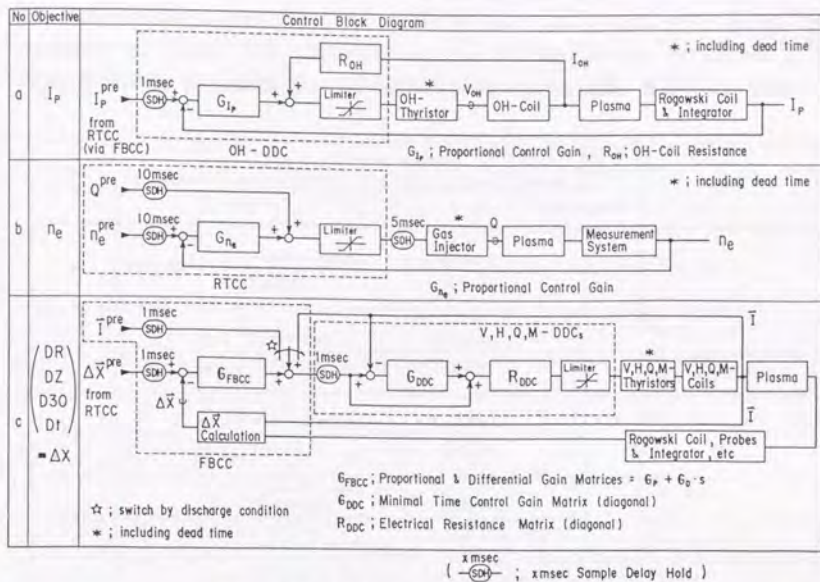


Fig. 3.1 Block Diagram of Feedback Control

Now we discuss these control methods from the view point of time advancement, commonly there are 2 or 3 periods corresponding to the procedures.

- (1) Around the ignition (from $t=0$ to approximately 100 ms), during which the plasma current abruptly varies, many magnetic signals do not settle and error magnetic fields are induced to a large extent. In addition, the plasma-wall interaction does not settle. For fear that feedback control should harm the plasma, only preprogrammed control is performed in this period.
- (2) After the plasma current reaches a certain level(after $t=100$ ms), which depends on the applied one-turn voltage at ignition, feedback control is commenced.
- (3) At the end of discharge when the plasma current is decreased, feedback control on some coils has to be stopped. This reason is the same as (1). These are dynamically switched according to the preset schedule or the decision of the RTCC, FBCC and DDCs, shown in Fig. 3.2.

During the BUP, a preprogrammed OH-coil voltage is applied in order to control the loop voltage according to the ramp-up rate of I_p . A fully

preprogrammed control of the V-coil during the BUP was thought to be impractical since conditions are variable and too much effort would be required to "tune" DR. Instead, control of the V-coil in which I_v is proportional to the actual plasma current, $I_v = \alpha_v \cdot I_p$, was adopted. The relation

State Variable	Actuator	Control Method		out of control	Note
		Parameter	Gate Block		
I_p	OH-Coil	*1 Preprogrammed $V_{OH}(t)$	Feedback $I_p(t)$		
DR	V-Coil	*1 Proportion to I_p $I_V(t) = \alpha_V \cdot I_p(t)$	Feedback DR(t)		*3 α_V ; constant value I_p ; actual I_p
DZ	H-Coil	*1 Preprogrammed $I_H(t)$	Feedback DZ(t)		*3
D30	Q-Coil	*1 Preprogrammed or Proportion to I_p $I_Q(t)$ or $I_Q(t) = \alpha_Q(t) \cdot I_p(t)$	Feedback D30(t)	*4 $I_Q = 0$	*3, *6 $\alpha_Q(t)$; preprogrammed I_p ; actual I_p
Dt	M-Coil	*1 Preprogrammed or Proportion to I_p $I_M(t)$ or $I_M(t) = \alpha_M(t) \cdot I_p(t)$	Feedback Dt(t)	*4 $I_M = 0$	*3, *6 $\alpha_M(t)$; preprogrammed I_p ; actual I_p
n_e	Gas Injector	*2 Preprogrammed $Q(t)$ (gas flow rate)	Feedback $n_e(t)$	*5 Prepro- grammed $Q(t)$	*6
—	NBI	Preprogrammed PNBI(t) (power)			
—	RF	Preprogrammed PRF(t), $\phi_{RF}(t)$, $f_{RF}(t)$ (power)(phase) (frequency)			

- *1: Before $t=0$ each coil is excited to the preset current for cancellation of error fields.
 - *2: Initial gas is fed into the vessel according to the preprogrammed $Q(t)$.
 - *3: DDCs always control their thyristors to track the coils' currents using the minimal time control algorithm.
 - *4: When $I_p < 500$ kA or $DR < -10$ cm (limiter configuration)
 - *5: If n_e measurement system misses the data in case of trouble.
 - *6: From $t=0$ to the end no feedback control operation can be selected.
- ∇ : Control methods are switched by the time oriented trigger. Each timing can be independently set as a discharge condition.
 Υ : Control methods are switched by the event oriented trigger.
 A(t): It denotes parameter 'A' depends on time.

Fig. 3.2 Time Chart of Dynamical Switching of Control Methods

between I_v and I_p is easily derived from the analytical equilibrium solution of Shafranov equation on the rough supposition that the beta value, plasma internal inductance and DR are constant. The effect of eddy current has to be taken into consideration of α_v value. The I_v control cycle was adopted to be 0.5 msec during this period.

The JT-60 device is nominally symmetric about the mid-plane of the vessel. However, errors in the placement of the coils generate stray horizontal fields which are cancelled by the H-coil to maintain vertical position through DZ feedback control.

D30 and Dt control are indispensable for a divertor plasma in JT-60. The Q-coil as an actuator to D30 is controlled according to the preprogrammed current waveform. In addition to the Q-coil current (I_Q) waveform, a $\alpha_Q(t)$ waveform can be used to control I_Q in proportion to the actual I_p ($I_Q = \alpha_Q(t) \cdot I_p$). When the configuration is changed from divertor to limiter at the termination process of discharge, feedback control is stopped (I_Q is controlled to be 0 A). Dt control is the same as that for D30.

3.3 Pipeline System Estimation

A digital discrete control system essentially involves a dead-time element which depends on the program steps. The thyristor convertor also has a dead time which depends on the number of different parallel phase thyristors. Besides the dead-time (τ_d) element, the system characteristics is determined by the sampling interval (τ_s). τ_d and τ_s are sensitive to the phase crossover frequency and gain margin in the Nyquist diagram, respectively. Their quantitative estimation against τ_d and τ_s depends on the order and linearity of the system.

Supposing that the system is simply a linear and first order differential system with its amplitude of unity and time constant T, Corresponding to a coil circuit. The block diagram can be described in Laplace transformed region in Fig. 3.3. The total transfer function $G^*(j\omega)$ is not $G(j\omega)$, because G^* involves spurious components of $G(j\omega + 2\pi jn/\tau_s)/\tau_s$. Then

$$G^*(j\omega) = \frac{1}{\tau_s} \sum_{n=-\infty}^{+\infty} G(j\omega + j \cdot n \cdot \frac{2\pi}{\tau_s})$$

The Nyquist diagram of $G^*(j\omega)$ gives a rough estimation on the gain margin and phase crossover frequency on the pipeline system with τ_s and τ_d .

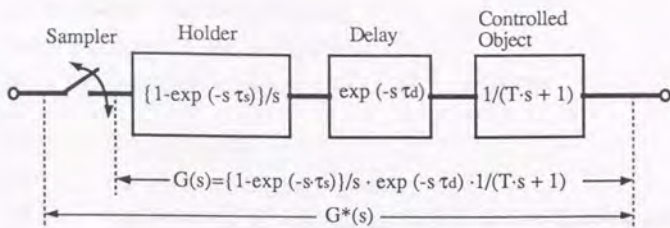


Fig. 3.3 Block Diagram of Pipeline System

4. Calculation of Plasma Equilibrium Parameters

How we obtain plasma equilibrium parameters in JT-60 is described in this section. I_p is directly measured by the integration of the Rogowski coil voltage. Other equilibrium parameters are calculated from 6 pairs of magnetic probes. A pair is composed of probes in the r and w directions. They are located at intervals of 60 degrees poloidally in the same poloidal plane inside the vessel. In the calculation method with only probes, we have first to define the center of plasma. We define it as the center of the outermost magnetic surface instead of the weight center of I_p calculated by a multiple moment algorithm^[2]. The reason is that the latter is very sensitive to the Shafranov Lambda Λ ($\beta_p(\text{poloidal beta}) + l_i$ (corresponding to the internal inductance)/2 - 1). The 1st order Fourier components B_p and B_w of the poloidal magnetic field is calculated from the poloidal flux function of Mukhovatov and Shafranov^[3]. Elimination of Λ using B_p and B_w expressions gives DR expression^[4]. DZ is obtained by a multiple moment algorithm. Analytical expressions for D30, Dt and Λ are so complicate that statistical expressions were composed^[5]. Their coefficients were calculated using the least square processing of a data base of equilibria. The final expression for parameter y (=DR, DZ, D30, Dt or Λ) is

$$y = \sum_{j=1}^6 \left\{ (A_j + B_j \cdot Z) \frac{B_{\theta j}}{I_p} + (C_j + D_j \cdot Z) \frac{B_{\omega j}}{I_p} \right\}$$

where $Z = I_M/I_p$ (DR, DZ, D30 and Dt cases) or I_Q/I_p (Λ case), B_p/ω_j is the actual magnetic flux intensity at the j -th probe location, and A_j , B_j , C_j and D_j are constant coefficients.

Furthermore, precise calculation requires the correction of probe/Rogowski coil orientation and stray toroidal flux coupling. The following calculations are also performed in real time in the fast array procedures (Zip3216)^[6]:

$$\begin{aligned}
 B_{\rho j} &= F1j \cdot \hat{B}_{\rho j} + F2j \cdot \hat{B}_{\omega j} + F3j \cdot DI_T, \\
 B_{\omega j} &= F4j \cdot \hat{B}_{\rho j} + F5j \cdot \hat{B}_{\omega j} + F6j \cdot DI_T, \\
 I_p &= k1 \cdot \hat{I}_{Rog} + k2 \cdot \hat{I}_V + k3 \cdot \hat{I}_H + k4 \cdot \hat{I}_Q + k5 \cdot \hat{I}_M + k6 \cdot DI_T,
 \end{aligned}$$

where

$$\begin{aligned}
 DI_T &\equiv I_T(t) - I_T(0), \\
 I_T(t) &: \text{the observed TF coil current,} \\
 I_T(0) &: \text{the observed TF coil current at the time-integration start time,} \\
 \hat{B}_{\rho j}, \hat{B}_{\omega j} &: \text{the observed } j\text{-th } \rho/\omega \text{ probe signals,} \\
 \hat{I}_{V/H/Q/M} &: \text{the observed V/H/Q/M-coil current,} \\
 \hat{I}_{Rog} &: \text{the observed Rogowski coil current, and} \\
 F_{ij}, k_i &: \text{the constant coefficients.}
 \end{aligned}$$

5. Performances of Plasma Control

Minimal-time control gains in the DDCs were, at first, calculated using a one-circuit model, excluding mutual couplings and eddy currents, and were checked in coil excitation tests. Actual gains were found to be 1/4-1/8 of the theoretical ones.

The coil arrangement in JT-60 was carefully designed so that the set of windings of each coil should generate a uniform magnetic field which approximately acts on one equilibrium parameter. Thus, initially equilibrium control is roughly regarded as a 1-input/1-output system. The gain calculation methods for such a system depend on their criterion of evaluation. A rough estimation is as follows:

- (1) To add the feedback route whose transfer function is set $F(s)$ to the system shown in Fig. 3.3.
- (2) To compose the closed loop system; $A(s) = G^*(s) \cdot F(s) / \{1 + G^*(s) \cdot F(s)\}$.
- (3) To set the criterion that $A(j\omega)$ has to have a break frequency of about 20 Hz in its Bode diagram.
- (4) To tune $F(s)$ ($F_P + F_D \cdot s$, in PD control) to satisfy the criterion.

In the commissioning with plasmas, the gains were tuned from the initial estimated ones.

In actual experiments this system controls the parameters passably using only diagonal and constant (independent of phases) gain matrix G_{FBCC} . This is seen in Fig. 3.1(a). As only proportional control is applied for I_p control, the bias between commands actual values was of concern, but fortunately it was very small. The accuracy is about 20 kA at $I_p = 3.2$ MA, as shown in Fig. 5.1.

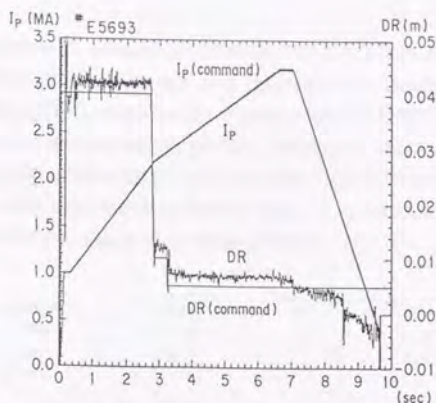


Fig. 5.1 I_p and DR Waveforms Compared with their Commands

As the time lag of gas feed is very long (about 100 msec), high gain feedback control on n_e cannot be realized. Therefore, a slight swelling of n_e waveform was observed. The accuracy is about 10% at $n_e = 3 \times 10^{13}/\text{cc}$.

The $I_v = \alpha_v \cdot I_p$ control was found to be effective for DR control in BUP. Though the α_v value naturally depends on the ramp-up rate of I_p , plasma internal parameters and induced eddy currents, even a constant value is effective. Since the eddy currents disturb the penetration of vertical magnetic field, the phase of this system is behind. Therefore, differential control was added to the proportional control for phase advancement of the system and this improved the DR control characteristics. The accuracy is about 4 mm at $I_p = 3.2$ MA flat top, as shown in Fig. 5.1.

DZ is originally stable in circular cross-section plasma, and its control accuracy is about 2 mm at $I_p = 3.2$ MA flat top. The accuracies of D30 and Dt control are about 1 mm and 3 mm at the $I_p = 1.0$ MA flat top, respectively.

6. Emergency Termination of Discharge

During normal operations, plasma contains substantially electromagnetic and thermal energy which could be released to the vacuum vessel in case of abnormal events, such as disruptions, run-away modes, etc. To avoid such events, methods for the emergency termination of the discharge were developed for JT-60. Three types are prepared corresponding to the level of emergency: Soft landing, C-stop and D-stop. In addition, N-stop was prepared for the protection of the energized PF coil power supplies.

(1) Soft landing

In discharges with additional heating NBI, for fear that the neutral beam should pass through the plasma and damage the beam armor plate in the opposite side, the RTCC receives the plasma density from the diagnostic system to check whether or not the target plasma density is adequate. If not, the RTCC terminates the plasma discharge without additional heating. Thus, the RTCC judges the plasma and device status and, if necessary, it terminates the discharge by shifting to the soft landing phases.

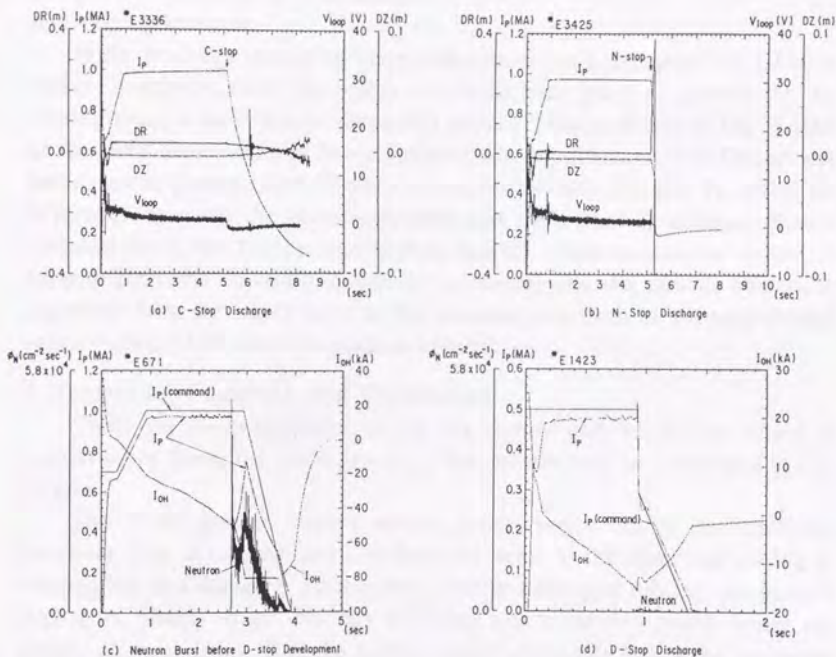


Fig. 6.1 Emergency Termination of Discharge

(2) C(control)-stop^[7]

When the TF coil power supply detects a failure and starts to demagnetize the TF coil, the FBCC is required to control the plasma position and shape until the plasma current terminates according to its time constant. In the C-stop, control is restricted to the plasma equilibrium parameters. Figure 6.1(a)

shows an example of a C-stop. In this example, it took 2 s to decrease I_p from 1 MA to 0.1 MA.

(3) N(natural)-stop

This type of plasma termination is mainly aimed at the protection of the PF coil power supply. When PF coil power supply detects its own abnormal state, it places thyristors in bypass-pair mode. Coil currents and plasma current decrease, interacting with each other. Figure 6.1(b) shows an example of an N-stop. About 150 msec after the N-stop began, the position started to move outward and finally the plasma disrupted.

(4) D(disruption)-stop

If the feedback control of plasma current is not interrupted, the OH-coil power supply makes an effort to raise the plasma current to its preprogrammed level after a disruption occurs. This is shown in Fig. 6.1(c). At the same time, bursts of X-ray and neutrons are observed. The D-stop was developed to prevent this. When a disruption is detected, that is, when the difference between the preprogrammed and the actual I_p is bigger than a specified level, the D-stop algorithm is applied which causes the control to jump to IDP (the " I_p -damping-phase" reference) and the plasma current is decreased from its actual value at that moment, not from its preprogrammed value. Figure 6.1(d) shows a resultant example.

7. Remaining Problems and Discussions

There are many problems on plasma control and we do not intend to discuss all of them, but some aspects of our interest will be mentioned in this section.

The JT-60 plasma control system satisfactorily fulfills its functions. However, Fig. 5.1 shows that DR does not agree to the command during I_p ramping-up and damping. Furthermore, during additional heating, parameters such as Λ , plasma shape, etc. vary to a large extent and they could change the plasma characteristics. Thus the system cannot adequately follow the variations of a plasma. As far as Λ problem is concerned, it plays such an important role in the plasma characteristics that its controllability must be paid attention. As OH-coil voltage, gas flow-rate, RF power, etc. affect it, they are candidates as control variables for Λ ^[8,9]. Thus state equations for concerned equilibrium parameters should be analytically or experimentally found at first, then proper control method have to be developed and applied. It is natural that the precise calculation of parameters should be required. Of course, how to determine the plasma controlled parameters is one of big problems, but we do not discuss the problem here.

Once the relations between magnetic field and controlled parameters are obtained as linear or nonlinear formulas, the relations between magnetic field and the external coil current/voltage still remain a complicated problem, arising from the existence of eddy currents and mutual couplings of coils. Static one-to-one correspondences do not hold during the transient phases of a discharge. A multi-variable control method is then required. We have to solve the transient problem on (non-)linear, multi-variable system. This does not allow easy calculation of gain, as opposed to a 1-input/1-output system. Adequate understanding of the multi-variable system is necessary. In particular, eddy current analysis comes up as a major problem. It has been investigated in many ways, but the methods themselves are still being discussed. In addition, the plasma movement induces the voltage/current in the coils and vessel which makes the problem more difficult. Analysis of these dynamical systems cannot be avoided on the way to the optimization of a plasma control system.

After the state equations are completely expressed in certain formulas, the control method has to be investigated next. If nonlinearity is not so strong, any set of equations may be converted to simultaneous 1st order differential equations along the nominal trajectory. We must then consider many problems in linear control theory such as system stability, internal state observer, reduction of a large scale system, optimal gains for a discrete time-delayed system, etc. Each problem involves elements peculiar to tokamak plasmas. In moving toward the design of a fusion reactor, the methodology for solving these problems must become much more sophisticated. We believe that we are now at the starting point.

8. Concluding Remarks

The JT-60 plasma control system contributes to the production of expected plasmas. Many problems, however, still remain to realizing optimal plasma control. Both the elucidation of the plasma behavior and the methodology of the approach, theoretical or phenomenological, will be important for the future design of plasma control systems.

References in Chapter IV.1

- [1] I. Kondo et al., "The JT-60 central control system," *Fusion Engineering and Design* vol.5 (1987) No.1.
- [2] H. Aikawa et al., Derivation of plasma displacement in a tokamak from magnetic probe signals, *Japanese Journal of Applied Physics* vol.15 (1976) pp.2031-2032 and p. 2479.
- [3] V.S. Mukhovatov and V. D. Shafranov, Plasma equilibrium in a tokamak, *Nuclear Fusion* vol.11 (1971) No.6.
- [4] D.E. Voss et al., Application of numerical equilibrium calculations to positioning of the Princeton Large Torus plasma, *Princeton Plasma Physics Laboratory Report No.1483* (1978).
- [5] N. Hosogane et al., Method for measuring divertor configuration parameters for feedback control in JT-60, *Nuclear Fusion* vol.26 (1986) No.5.
- [6] T. Kimura et al., Application of the fast array processor for JT-60 plasma control, *Proceedings of 14th Symposium on Fusion Technology, 1986, Avignon, France.*
- [7] K. Kurihara, et al., "Dynamics of plasma current control system in JT-60," *Proceedings of 12th Symposium on Fusion Engineering, 1987, Monterey, USA.*
- [8] R.J.Hawryluk et al., "The effect of current profile evolution on plasma-limiter interaction and the energy confinement time," *Nuclear Fusion* vol.9 (1979) No.10.
- [9] K. Toi et al., Current density profile control by programming of gas puffing and plasma current waveform in the JIPP T-II tokamak, *Nuclear Fusion* vol.19 (1979) No.12.

IV.2 Plasma Control System for the JT-60 Upgrade with Multiple Processors (1991-)

1. Introduction

JT-60 tokamak was reconstructed in 1989 to change the vacuum vessel and poloidal field configuration. This aims at improving plasma performances, whose major different points are as follows:

- (i) The plasma configuration is changed from a circular outside/lower-divertor plasma with the volume of 60 m^3 to an elongated lower-divertor one with that of 110 m^3 , as shown in Fig. 1.1.
- (ii) The rated plasma current is increased from 3.4 MA to 7.0 MA.
- (iii) The duration of the pulse discharge is extended from 10 sec to 15 sec.

These differences in JT-60 Upgrade^[1] (hereafter, JT-60U) make big influences on the plasma control system as follows: An elongated plasma is positionally unstable. However, horizontal poloidal field induced by plasma vertical motion tries to restore a plasma. Fast feedback control could make a plasma stable. In the severest case of a JT-60U plasma with its ellipticity of 1.6, the control cycle for the vertical displacement is required to be less than 0.5 msec and the allowable dead time in control system is ~ 1 msec, according to the rough estimation. This requires much faster computation for the horizontal field coil feedback control. For fear that a high current plasma disrupts because of lack of control accuracy, floating point calculation is required to improve the precision of control. The extension of plasma discharge duration requires the computer to have much larger addressed space than 16-bit one.

Furthermore, the plasma control system in 1985~1989^[2] have several problems; (a) the data transfer rate via the GPIB (General Purpose Interface Bus: IEEE standard 488) interface, used for data communication from the fast array processor to CAMAC, is slow (several kbytes per second), (b) In the data transfer from the fast array processor to the minicomputer HIDIC-80E, made by Hitachi Co. Ltd., digital-to-analog conversion is done in the fast array processor, and analog-to-digital conversion is done in HIDIC-80E. These digital-analog-digital conversions includes large error, and (c) the fast array processors can perform only 16-bit integer calculation. The division calculation is then computed using tabulated "look-up" data, and often includes large error.

The requirements and solutions of the problems obliged the plasma equilibrium control system (see dotted square in Fig. 2.3 of Chapter IV.1) to be almost completely reconstructed. Then, the more sophisticated system for

plasma equilibrium control was tried to be made on the basis of the operational experiences.

The first step of system design is to determine rough configuration. The following decision is made: New plasma control system is mainly constituted by VME standardized (VERSA Module Europe: IEEE. standard P-1014) modules. These have several good features;

- (i) the VME standardized bus speed is fast up to 20 MHz,
- (ii) the fastest processors can easily supersede the old ones on the same place in the VME-bus without changes of other system configuration,
- (iii) many companies supply the modules, which results in that the appropriate prices are always set,
- (iv) if a code is programmed in popular languages such as C, Fortran, then the code can work on a new processor with only change of the compiler for the new processor, and
- (v) the data communication between VME and CAMAC is possible. The existing CAMAC modules can also be involved in the system by linking with VME modules.

The other steps of system design will be discussed in the following section.

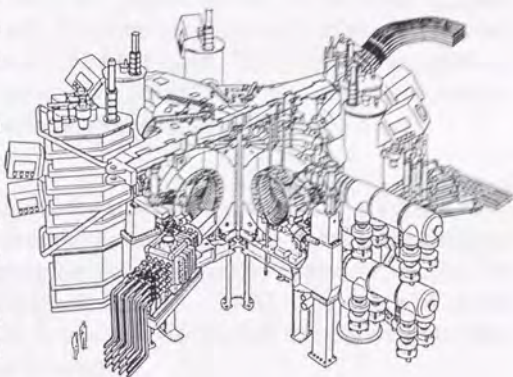


Fig. 1.1 JT-60 Upgrade Cutaway View

2. Requirement Analysis

The detailed requirements are considered from the view point of the basic design concept for a plasma control system. In other words, the answer to the following question is then discussed: what is the indispensable performance and function for a tokamak plasma real-time control system?

(1) Fast calculation

To suppress the vertical instability of the JT-60U elongated plasmas, and to perform various kinds of real-time programs, a fast computer is required more acutely this time than in the previous system. Naturally the fastest microprocessor of that moment must be adopted. Furthermore, to increase the program steps that can be executed within a certain period of time, parallel

and/or pipelined processing should be introduced in the system. (The evaluation of pipelined process is discussed in the appendix.) Consequently, in JT-60U, three microprocessors are equipped on the same (VME) bus and work in parallel. In addition, five controllers for PF coil power supplies together with the 3 processors perform feedback control as a pipeline system.

(2) Different control cycles

In general, control cycles are determined by the time constants of controlled objects. Though controls for different time constants require different control cycles, the sufficient shortest control cycle is usually chosen for the only one clock cycle. On the contrary, the longer control cycle makes more room for calculations, which gives the better situation for development of the program. In JT-60U, control for plasma vertical displacement requires the shortest cycle, while controls for other quantities such as plasma current, its horizontal displacement allow the longer cycle. Three clocks with different control cycles should be then generated. Five different time delays with respect to the different clocks should also be necessary for pipelined processing.

(3) Fast result data transfer

The short control cycle inevitably increases the amount of the result data. The fast data transfer is then required for fast evaluation of experimental data. Hardware and software necessary for fast data transfer should be selected. In JT-60U, the CAMAC-standardized module, "ACD," having a 4-kbyte communication buffer memory is used to link the fast microprocessors with the supervisory discharge control computer.

(4) Wide flexibility for control methods

To find a proper plasma control method corresponding to the plasma condition is one of the most important objectives in the experiments. The flexible structure of plasma control is then expected to enable the trial and error of the control methods. In addition, the dynamical switching of control methods during a pulse of discharge are required for the better plasma operation. In the RF current drive experiment, for example, plasma current feedback control using the ohmic heating coil should be changed to constant current control, in order to examine the RF effect, while RF wave is being radiated into the plasma.

Both flexible structure and dynamical switching of plasma control methods are built in the system. To provide against the requirement, the set composed of many patterns of control algorithms is newly introduced. The

patterns of the control algorithms are registered in the real-time processors prior to the experiment and the time evolution of the pattern number is preprogrammed as a waveform. The real-time program can also change the pattern number in real time, and many patterns of control algorithms can be registered as far as the processor memory area remains. This method thus gives much wider flexibility than the previous system.

(5) Simplification of the system—on the basis of the operational experiences

The operational experiences in 1985–89 result that the following simplifications of the system functions are possible:

(a) The system for plasma equilibrium control should become a real-time control supervisor in place of that for plasma particle supply and heating control. It is because plasma equilibrium control makes necessary preparations

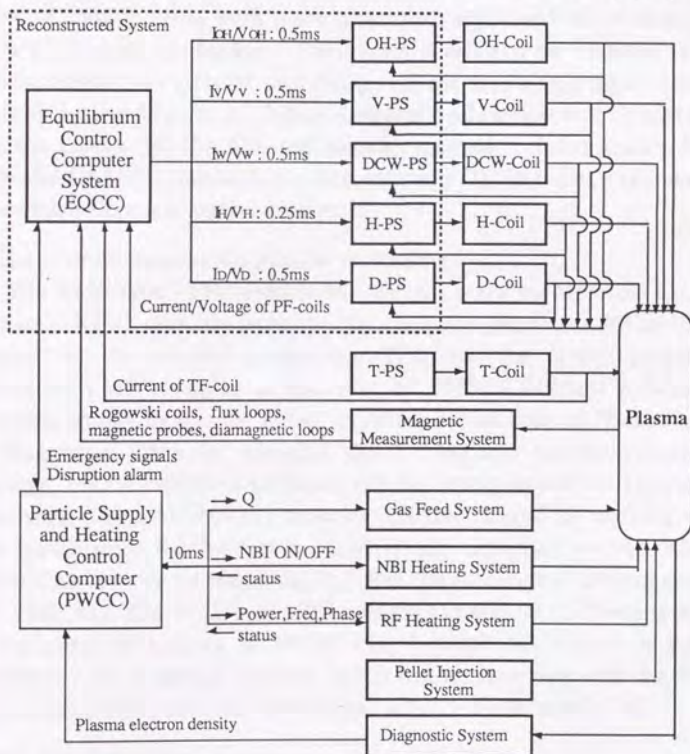


Fig. 2.1 Data Flows in the JT-60U Plasma Control System

for other plasma operations with top priority. The resultant real-time data flow is shown in Fig. 2.1.

(b) To cut short a pulse length of discharge in case that disruption is occurred and to change the feedback control gains are the useful functions that have been actually often utilized in the past JT-60 experiments.

(c) Two patterns of control for each PF-coil power supply, voltage and current regulations, can be switched at any timing in real time. This is one of the features that the digital controllers originally have.

How the requirements described above are realized in the plasma control system shall be clarified in the following sections.

3. Hardware Configuration

On the way to the completion of system design, several decisions of hardware configuration were made after investigations with or without tests for performance evaluation. These decisions are as follows: (1) The microprocessors for parallel processing, (2) the fast signal input system, (3) the clock system to generate different control cycle clocks and different delays from the clocks, (4) the fast data transfer method (communication between VME and CAMAC standardized modules), and (5) the better environment for software development and maintenance.

(1) The microprocessors for parallel processing

The VME-type CPU modules MVME181, made by Motorola Co., which contains a RISC (Reduced Instruction Set Computer) processor MC88100 were adopted for the parallel processing. This was the fastest processor of obtainable VME modules at the year of 1989. Computer technology is advancing so rapidly that the fastest processor cannot keep its "fastest" position for long time. Then by adopting the C language for the programming language, once-established software can be "transplanted" in alternation of processors. Three MVME181 modules (CPU#1, 2 and 3) working with 20 MHz clock with 8-Mbyte core memory are equipped on the VME bus (MVME181 is made by Motorola Co.). But this module can communicate with only VME bus. The VME-type CPU module MVME147 (CPU#0) is equipped for the program loading to MVME181, because MVME147 is based on MC68030 with 4 Mbytes DRAM and it has an interface with the Ethernet (IEEE standard 802.3) network (MVME147 is made by Motorola Co.).

(2) The fast signal input system

A digital integrator VME module (up-down counter, UDC) was newly

developed for time-integrals of voltage-to-frequency converted signals of electromagnetic sensor (UDC802, manufactured by MTT Co. Ltd.). A VME-type analog-to-digital convertor (ADC), was also newly developed (MVME2012, manufactured by MTT Co. Ltd.). The 18 UDCs and 2 ADCs are equipped on the same VME bus with CPUs. As one word/channel in the UDC is composed of 16 bits, two data (32 bits) are simultaneously collected by the CPU via VME bus 32-bit data line.

(3) The clock system to generate different control cycle clocks and different delays from the clocks

The clocks of three different cycles are generated for pipeline processing. The basic clock with the cycle time of 1 msec is generated from the existing CAMAC standardized CPG (Clock Pulse Generator). A VME-type CPG module that produces three clocks of different cycles is newly developed (CPG241, manufactured by MTT Co. Ltd.). This module can produce the clocks with three periods of $T/2^{n1}$, $T/2^{n2}$ and $T/2^{n3}$, where T is the cycle of the received basic clock (for example, 1 msec), and $n1$, $n2$ and $n3$ are the integer values.

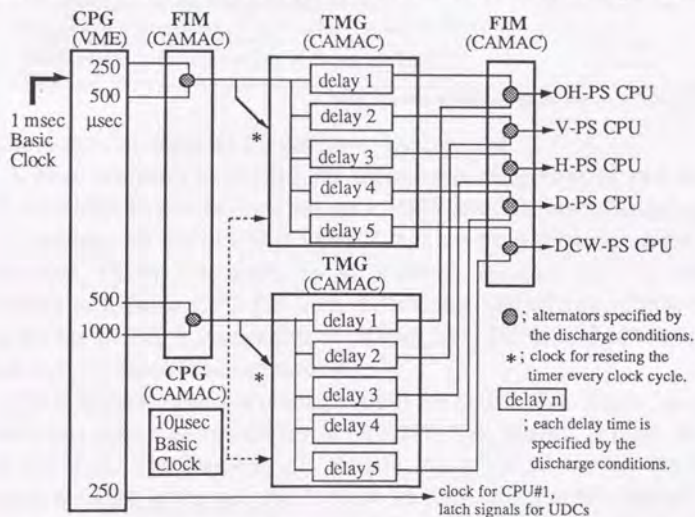


Fig. 3.1 VME-CAMAC Timing System Configuration to Produce the Five Clocks Independently Delayed from the Two Different Master Clocks

The delayed clocks are easily produced by the combinations of CAMAC standardized modules. Figure 3.1 illustrates how the delayed clocks are generated by the combination of CAMAC and VME modules. A fan-in module

(FIM) is used for the selector of input signals. A timing generator (TMG) makes delayed pulses in preset time intervals from the trigger pulse.

(4) Fast data transfer

The 24-bit command messages in the real-time pipelined process are transferred to the controllers of PF coil power supplies every control cycle via a CAMAC module. The discharge result data of up to 6 Mbytes should be transferred to the supervisor, having only a CAMAC interface, soon after the pulse of discharge. Fast VME-CAMAC communication is then necessary. As a result of the performance tests^[3], the linkage of VME with CAMAC via CAMAC branch highway shows the faster data transfer (2.5 μ sec/3 bytes) than the 8-bit parallel bus (7.5 μ sec/3 bytes), as shown in Table 3.1. Finally, a CAMAC branch driver, CBD, is equipped on the VME bus to communicate with the 24-bit buffer module (ACB) and the 4-kbyte buffer module (ACD) via the type-A2 crate controller (CCA2).

Table 3.1 Comparison of the VME-CAMAC communication speeds

Communication Route: Module (VME/CAMAC)	Elapsed Time (3 bytes)
CBD (VME) \rightarrow ACB (CAMAC) :	2.5 μ sec
CPBI (VME) \rightarrow PBCC(CAMAC) \rightarrow DPMD (CAMAC) :	7.5 μ sec

Note: Module specifications are shown in Table 3.2.

(5) The better environment for software development

A host computer is needed for software development of two kinds of CPUs (MVME181 and 147) on the same VME bus. The compiler/debugger of the C language for MC88100 (CPU#1,2 &3) has been released on the SUN3 workstation. (SUN 3 is made by SUN Micro Systems Co.). In addition, MC68030 is a main CPU for both SUN3 and MVME147 (CPU#0). The compiler for SUN3 is compatible to MVME147. SUN3 and MVME147 are linked with the same Ethernet network.

UNIX is the standard operating system for SUN3. "Vx Works" is used as the real-time operating system for MVME147. "Vx Works" is made by Wind River Co. Ltd. The function of "remote log-in" available on the UNIX-Ethernet network gives program edition environment for MVME147 at the SUN3 terminal. The supervisor of the PF-coil power supply, AS3260 (fully compatible to SUN3), is linked with this Ethernet network, where AS3260 is made by Toshiba Corp. The result data from the PF-coil power supply is transferred to MVME147 via this network, and MVME147 transferred the data to the existing CAMAC-HIDIC 80E system (see Chapter IV.1).

The hardware configuration of the JT-60U plasma equilibrium control system based on the foregoing discussion is shown in Fig. 3.2 and the VME and CAMAC module specifications are presented in Table 3.2.

Table 3.2 VME and CAMAC Specifications

No	symbol	type	manufacturer (nation)	specification / performance
1	CPU #1,2,3 (VME)	MVME181	Motorola Co.(USA)	parallel processing in real time MC88100RISC, 20MHz, 8MB
2	CPU #0 (VME)	MVME147	Motorola Co.(USA)	on-line (non-real-time) processing MC68030, 20MHz, 4MB
3	SYSC (VME)	MVME050A	Motorola Co.(USA)	system controller for VME-bus
4	CPG (VME)	CPG241	MTT Co.(Japan)	clock pulse generator 1 msec to 0.25/0.5/1.0 msec clock
5	UDC#1-18 (VME)	UDC802	MTT Co.(Japan)	up-down counter (digital integrator)
6	ADC#1,2 (VME)	MVME2012	MTT Co.(Japan)	analog to digital converter
7	DIO (VME)	MVME340A	Motorola Co.(USA)	digital inputs and outputs
8	DAC (VME)	DT1403-4	Data Translation Co. (USA)	digital to analog converter analog output for monitoring
9	CBD (VME)	CBD8210	Creative Electronic Systems (Switzerland)	CAMAC branch driver 2.5 msec/24 bits
10	BR #1-6 (VME)	PTVME902A	Performance Tech. Inc. (USA)	VME-bus repeaters
11	CPBI (VME)	CPBI8216	Creative Electronic Systems (Switzerland)	VME-CAMAC parallel bus interface (8-bit parallel)
12	PBCC (CAMAC)	KS3922	Kinetic Systems Co. (USA)	CAMAC crate controller for parallel bus
13	DPMD (CAMAC)	NG-105	Kokusai Electric Co. (Japan)	dual port memory with D-ports (256-byte dual buffer memory)
14	ADC (CAMAC)	LY8212	LeCroy Co.(USA)	analog to digital converter
15	DO (CAMAC)	KS3082	Kinetic Systems Co. (USA)	isolated digital output
16	CCA2 (CAMAC)	CCA2/G	DSP Technology Inc. (USA)	type-A2 crate controller
17	ACB (CAMAC)	NA-103	Kokusai Electric Co. (Japan)	auxiliary controller with branch highway-ports (24-bit register)
18	ACD (CAMAC)	NA-104	Kokusai Electric Co. (Japan)	auxiliary controller with D-ports (4k-byte dual buffer memory)
19	FIM (CAMAC)	NF-013	Kokusai Electric Co. (Japan)	fan-in module (input signal selector)
20	TMG (CAMAC)	NI-002	Kokusai Electric Co. (Japan)	delayed timing pulse generator
21	CPG (CAMAC)	NI-102	Kokusai Electric Co. (Japan)	clock pulse generator for TMG (10 μ sec clock)

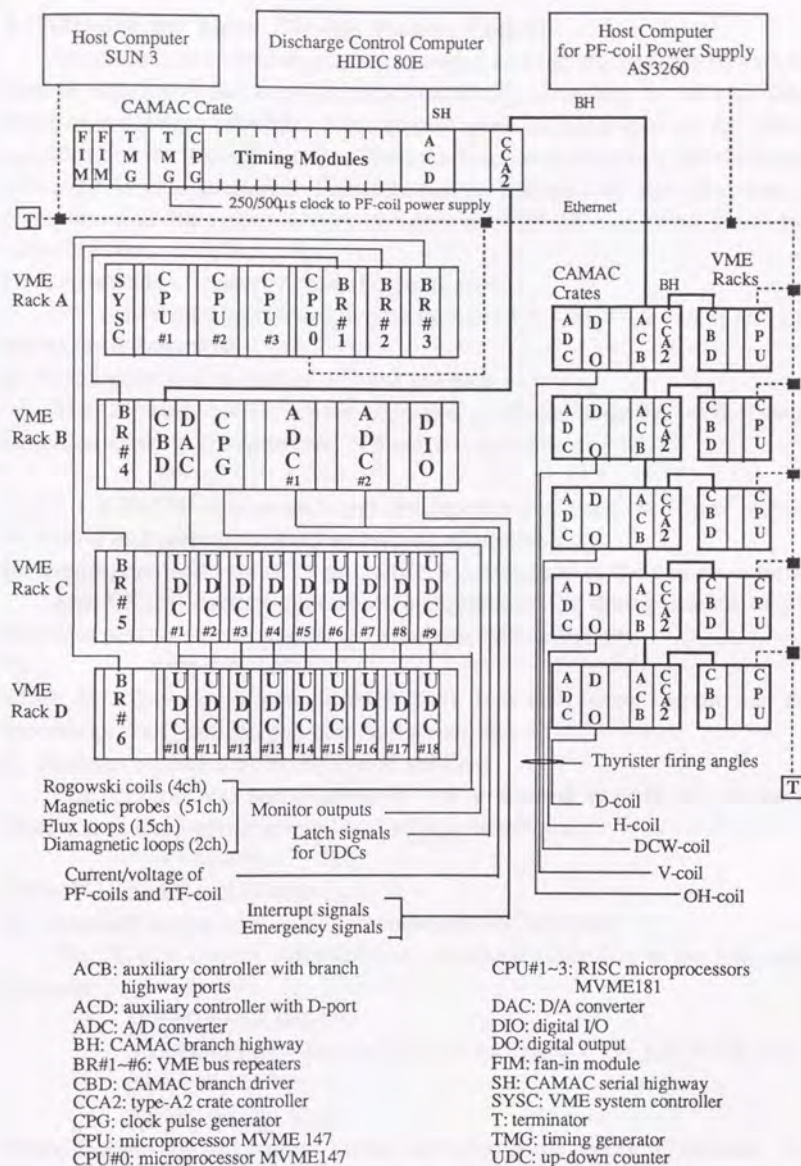


Fig. 3.2 JT-60U Plasma Equilibrium Control System
Based on VME Multiple Processors

4. Software for More Flexible Plasma Control

To obtain more flexible plasma real-time control, the patterns of various control algorithms can be switched dynamically according to the algorithm itself or the preset schedule. Such control must be supported by the safety operation for the tokamak system. Then the function to terminate the discharge smoothly is also prepared. This function is initiated by the detection of disruption and emergency events (the excess of PF-TF coil stress limits and other hardware troubles)

(1) Dynamical switching of control algorithms

The following algorithms are now registered in CPU#1, 2 and 3, and can be switched dynamically.

(a) Preprogrammed control of PF-coil currents

The PF-coil current commands are produced exactly in the same evolution as the preprogrammed coil current waveforms:

$$I^{com} = I^{pre},$$

where I is the PF coil current, and the superscripts "com" and "pre" denote command and preprogrammed waveform, respectively.

(b) Preprogrammed control of proportional coefficients to the plasma current

The PF-coil current commands are produced by multiplication of the observed plasma current and the preprogrammed coefficients:

$$I^{com} = C^{pre} \cdot I_p^{obs},$$

where C is the preprogrammed coefficient, I_p is the plasma current, and the superscript "obs" denotes the observed parameter.

(c) Preprogrammed control of PF-coil voltages

The PF-coil voltage commands are produced exactly in the same evolution as the preprogrammed coil voltage waveforms:

$$V^{com} = V^{pre},$$

where V is the PF coil voltage.

(d) Observed current plus deviation command for feedback

The PF-coil current commands are produced according to the following equation:

$$I^{com} = I^{obs} + \Delta X \cdot \mu_0 I_p^{obs},$$

$$\Delta X \equiv G_P \cdot \Delta Y(t) + G_D \cdot \{\Delta Y(t) - \Delta Y(t-\Delta t)\} / \Delta t + G_I \cdot \sum \Delta Y(t-i\Delta t) \cdot \Delta t,$$

$$\Delta Y \equiv Y^{ref} - Y^{obs},$$

$$Y \equiv (I_p, R_p, Z_p, Z_x),$$

where I is the PF-coil current vector, μ_0 is the permeability of vacuum, G_P , G_D and G_I are proportional, differential and integral control gain matrices, $Y(t)$ is defined as the vector Y at the time t , Δt is the control cycle, $\sum \Delta Y(t-$

$i\Delta t$) is defined as the summation of $\Delta Y(t-\Delta t)$, $\Delta Y(t-2\cdot\Delta t)$, ..., and $\Delta Y(t-L\cdot\Delta t)$, L is given prior to the experiment, the superscript "ref" denotes the preprogrammed reference parameter, and R_p , Z_p and Z_x are the plasma horizontal position, vertical position and X-point vertical position, respectively.

(e) Observed voltage plus deviation command for feedback

The same as (d), by replacing current with voltage.

(f) Preprogrammed current plus deviation command for feedback

Almost the same as (d), except the equation:

$$I^{com} = I^{pre} + \Delta X \cdot \mu_0 I_p^{obs}$$

(g) Preprogrammed voltage plus deviation command for feedback

The same as (f), by replacing current with voltage.

(h) Preprogrammed coefficients multiplied by the observed plasma current plus deviation command for feedback

Almost the same as (d), except the equation:

$$I^{com} = C^{pre} \cdot I_p^{obs} + \Delta X \cdot \mu_0 I_p^{obs}$$

where C^{pre} is the preprogrammed coefficient vector.

(i) C-stop control

This algorithm is executed in case of emergency. All commands to PF-coil power supplies are independently produced according to the following procedures, till the plasma current is completely terminated:

•OH-coil power supply: $V_{OH}^{com} = 0$.

•V-coil power supply: The control algorithm is changed to:

$$I_V^{com} = I_V^{obs} + G_{PV} \cdot (R_p^{ref}(t_c) - R_p^{obs}) \cdot \mu_0 I_p^{obs}$$

where $R_p^{ref}(t_c)$ is the preprogrammed reference value at the time t_c when C-stop control starts and G_{PV} is the proportional control gain for C-stop.

•H-coil power supply: The control algorithm is changed to:

$$I_H^{com} = I_H^{obs} + G_{PH} \cdot (Z_p^{ref}(t_c) - Z_p^{obs}) \cdot \mu_0 I_p^{obs}$$

where $Z_p^{ref}(t_c)$ is the preprogrammed reference value at the time t_c when C-stop control starts and G_{PH} is the proportional control gain for C-stop.

•D-coil power supply: The control algorithm is changed to:

$$I_D^{com} = \{ I_D^{obs}(t_c) / I_p^{obs}(t_c) \} \cdot I_p^{obs} + G_{PD} \cdot (Z_x^{ref}(t_c) - Z_x^{obs}) \cdot \mu_0 I_p^{obs}, \quad (I_D^{obs}(t_c) \geq 1 \text{ kA})$$

$$V_D^{com} = 0, \quad (I_D^{obs}(t_c) < 1 \text{ kA})$$

where $Z_x^{ref}(t_c)$ is the preprogrammed reference value at the time t_c when C-stop control starts and G_{PD} is the proportional control gain for C-stop.

•DCW-coil power supply: $V_{DCW}^{com} = 0$.

(j) Plasma current control

This is OH-coil voltage control according to the following equation:

$$V_{OH}^{com} = \min(V_{OH}^{req}, V_{OH}^{per}),$$

$$V_{OH}^{req} = I_{OH}^{obs} \cdot R_{OH} + \Delta V_{OH},$$

where V_{OH}^{per} is the permissible maximum voltage, $\min(a,b)$ is the operator to choose the smaller value of a and b , R_{OH} is the electric resistance of OH-coil, and G_{IP} is the proportional control gain with a dead band:

$$\Delta V_{OH} \equiv \begin{cases} G_{IP} \cdot (I_p^{ref} - I_p^{obs} - I_{DB}), & (I_p^{ref} - I_p^{obs} > I_{DB}) \\ 0, & (|I_p^{ref} - I_p^{obs}| \leq I_{DB}) \\ G_{IP} \cdot (I_p^{ref} - I_p^{obs} + I_{DB}), & (I_p^{ref} - I_p^{obs} < -I_{DB}) \end{cases}$$

where I_{DB} is a dead band width.

(k) Horizontal position control for the V-coil power supply

In case that eddy currents make a large influence on the horizontal position control in the current build-up period, the following control algorithms are prepared:

$$I_{V}^{com} = W_{1vpre} \cdot I_p^{obs} + W_{2vpre} \cdot V_{OHpre}, \text{ and}$$

$$V_{V}^{com} = K_{1vpre} \cdot I_p^{obs} + K_{2vpre} \cdot I_{OH}^{obs} + K_{3vpre} \cdot I_{V}^{obs} + K_{4vpre},$$

where $W_{1-2vpre}$ and $K_{1-4vpre}$ are the preprogrammed waveform based on the result of the computational analysis.

These control algorithms are usually switched according to the preset schedule. The switching of control algorithms can be preprogrammed for each PF-coil power supply independently, as shown in Fig. 4.1. This makes flexibility much wider than the previous system.

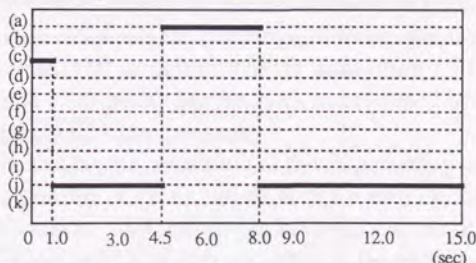


Fig. 4.1 An Example of the Preprogrammed Schedule of Algorithm Switching for OH-Coil Power Supply

(2) Gain switching

Feedback control gain matrices G_P , G_D and G_I are required to be time-variant to adapt the control system to the plasma states. In reality, it may be hard to preprogram the matrices from the operational point of view. The total time length of discharge is then divided into six periods, in which the fixed

matrices can be preset. The timing to switch the gain matrices can be arbitrarily determined by the discharge conditions prior to the discharge.

(3) Emergency termination

To cut short the pulse of discharge is the important method to avoid much severer damage to the tokamak devices, when the hardware/software troubles or plasma disruption occurs. Therefore, the total time length of discharge is divided into two periods; one is the plasma current build-up and plasma heating phase, and the other is the plasma current damping phase. If the emergency event is detected by the real-time controller CPU#1, 2 or 3, then all preprogrammed waveforms are skipped to the top of the plasma current damping phase.

(4) The pipeline time chart

The real-time feedback calculation procedures in a control cycle are as follows:

- (i) CPG produces and distributes the latch timing of signal integration to UDCs. This control cycle is usually set 250 μ sec.
- (ii) UDC interrupts CPU #1 to execute the own real-time program after the latch of signal integration.
- (iii) CPU #1 inputs the flux loops and Rogowski coil signals from UDCs via the VME bus.
- (iv) Every other control cycle at the completion of the data input, CPU#1 interrupts CPU#2 and #3 to execute the data input via the VME bus.
- (v) CPU#1 then calculates the plasma equilibrium parameters. Every other control cycle at the completion of the calculation, CPU#1 interrupts CPU#2 and #3 to permit the feedback computation with the CPU#1-calculated equilibrium parameter.
- (vi) CPU#1 calculates the commands to H-coil according to the assigned control algorithm. CPU#2 and #3 directly read the computer memory of CPU#1 via the VME bus and calculates the commands to OH-coil, V-coil, D-coil and DCW-coil according to the separately-assigned control algorithms.
- (vii) CPU #1, #2 and #3 output current/voltage commands to the PF coil power supply via the CBD module.

The pipeline system is composed of CPU#1, 2 and 3 together with the controllers of PF-coil power supplies. Figure 4.2 illustrates the pipeline time chart.

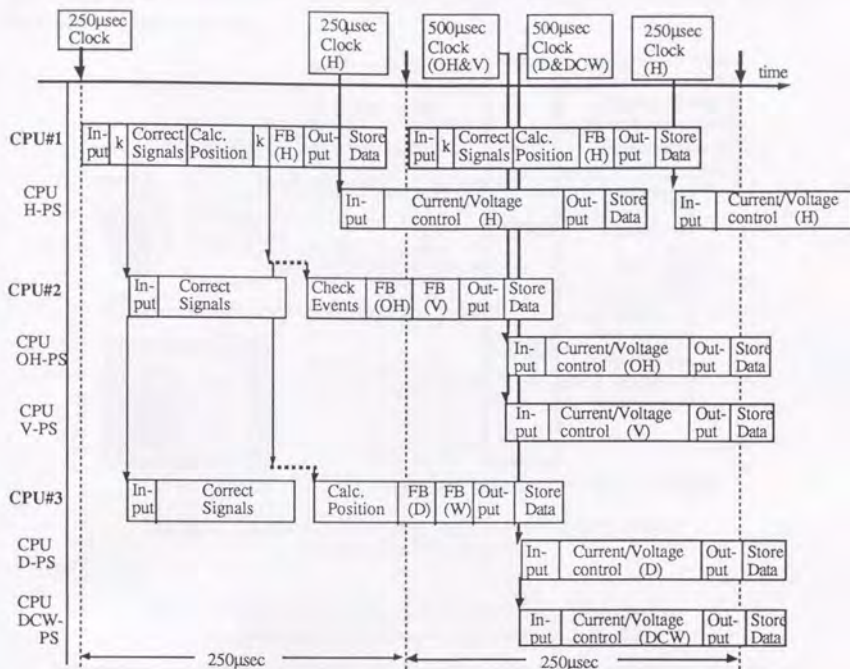


Fig. 4.2 Parallel and Pipeline Process Time Chart for JT-60U Plasma Equilibrium Control (k: flag setting, FB: feedback calculation)

5. Real-time Visualization of Plasma Shape

The plasma shape identification methods, proposed in Chapter II, can be utilized for real-time shape visualization with fast processors. Figure 5.1 and Table 5.1 show the system configuration and hardware specifications for real-time visualization. The upper VME-bus system in Fig. 5.1 is a simplified illustration of Fig. 3.3 and the lower one visualizes the plasma shape.

Formulas of the flux function value ϕ at a point x in the proposed methods are the same as:

$$\phi(x) = \sum C_i(x) \cdot I_{c_i} + \sum D_j(x) \cdot S_j, \quad (5.1)$$

where I_{c_i} & S_j are poloidal field coil currents and sensor signals (flux intensities, flux function values and plasma current), and C_i & D_j are coefficient functions of x . The design of a real-time visualization system composed of a microprocessor with a large memory containing C_i & D_j , a fast

This process does not require so fast computation as plasma feedback control. Approximately 25 msec is set for the cycle time of real-time visualization.

6. Concluding Remarks

The rebuilt plasma control system based on the VME modules works very well in the JT-60U operations and experiments. Highly elongated plasmas are also stably controlled by the 250- μ sec cycle feedback control. Therefore, the expected performances are completely attained, but several points to be improved are still remaining as follows:

- (i) The direct communication of different VME-bus systems is expected.
- (ii) To extend the distance between the VME-bus systems, data transfer by optical fibers is required. This also requires the signal conversion from parallel data to serial ones. Then a fast parallel-to-serial convertor is desired to be developed.
- (iii) The actual precision of analog-to-digital conversion is 10-bits at most with a 12-bit ADC. The more precise measurements are required for the better plasma control. A 16-bit or more ADC is expected.
- (iv) The larger data transfer and easier data handling requires the VME-to-network (Ethernet, for example) communication. This improvement will be technologically easy to be made.

References in Chapter IV.2

- [1] Horiike, H., et al., "Present status of JT-60 Upgrade," Proceedings of 13th Symposium on Fusion Engineering, p.1049, Knoxville(1989).
- [2] Kurihara, K., et al., "JT-60 plasma control system," Fusion Engineering and Design vol.11 (1990) pp.441-454.
- [3] Kimura, T., et al., "VME multiprocessor system for plasma control at the JT-60 Upgrade," Proceedings of Real-Time '89, IEEE Transactions on Nuclear Science vol. 36, No. 5 (1989) pp.1554-1558.

Appendix Pipelined control system evaluation.

Comparison of the pipelined and non-pipelined systems is discussed in this appendix. The pipelined system is defined in the discretized time domain as "the system having the shorter sampling interval than the delay time of the sampling interval." The non-pipelined system is then similarly defined as "the system having the equal (or longer) sampling interval to (or than) the delay time of the control system." A single processor system must belong to the non-pipelined system. The block diagram of the pipelined system is shown in Fig. A.1.

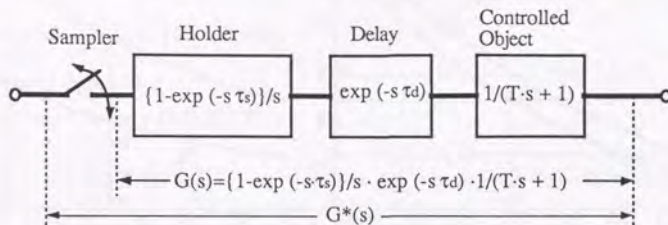


Fig. A.1. Block Diagram of the Pipelined System

In Fig. A.1, τ_s is the sampling interval, τ_d is the time delay, T is the time constant of the assumed controlled object, s is the parameter in the Laplace transformed region, and $G(s)$ and $G^*(s)$ is the transfer functions.

The transfer function $G^*(s)$ in the frequency domain ($s=j\omega$) must contain both the main component $j\omega$ and spurious components $j\omega + j \cdot n \cdot 2\pi/\tau_s$. Then

$$G^*(j\omega) = \frac{1}{\tau_s} \sum_{n=-\infty}^{+\infty} G(j\omega + j \cdot n \cdot \frac{2\pi}{\tau_s}) \quad (A.1)$$

To calculate numerically Eq. (A.1), the range of the summation is limited to $n = -10$ to $+10$. Now the time constants of two controlled objects are 5 and 10 msec. By reading the gain margins and phase crossover frequencies from the Nyquist diagrams of Eq. (A.1) for several τ_s and τ_d , comparison of the pipelined ($[\tau_s=1.0 \text{ msec}, \tau_d=1.5 \text{ msec}]$ and $[\tau_s=1.0 \text{ msec}, \tau_d=2.0 \text{ msec}]$) and non-pipelined ($\tau_s=\tau_d=1.0-1.6 \text{ msec}$) system responses is performed. The results are shown in Fig. A.2. The following observations are possible from Fig. A.2:

- (1) The gain margins in $[\tau_s=1.0 \text{ msec}, \tau_d=1.5 \text{ msec}, T=5 \text{ or } 10 \text{ msec}]$ and $[\tau_s=1.0 \text{ msec}, \tau_d=2.0 \text{ msec}, T=5 \text{ or } 10 \text{ msec}]$ do not deteriorate so largely as those in $[\tau_s=\tau_d=1.1 \text{ msec}, T=5 \text{ or } 10 \text{ msec}]$ and $[\tau_s=\tau_d=1.3 \text{ msec}, T=5 \text{ or } 10 \text{ msec}]$.
- (2) The phase crossover frequencies in $[\tau_s=1.0 \text{ msec}, \tau_d=1.5 \text{ msec}, T=5 \text{ or } 10 \text{ msec}]$ and $[\tau_s=1.0 \text{ msec}, \tau_d=2.0 \text{ msec}, T=5 \text{ or } 10 \text{ msec}]$ do not deteriorate so

largely as those in $[\tau_s=\tau_d=1.4 \text{ msec}, T=5 \text{ or } 10 \text{ msec}]$ and $[\tau_s=\tau_d=1.7 \text{ msec}, T=5 \text{ or } 10 \text{ msec}]$.

- (3) The phase crossover frequency is more sensitively influenced by the time delay of the pipelined system than the gain margin. ■

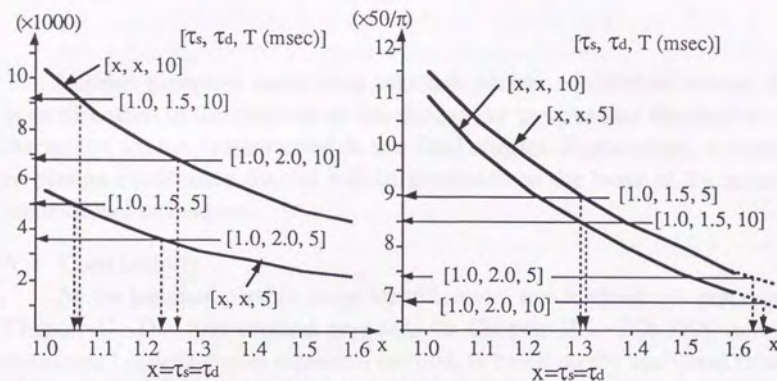


Fig. A.2 Gain Margins and Phase Crossover Frequencies in the Pipelined and Non-pipelined Systems.

Chapter V

Concluding Remarks

Various problems concerning tokamak plasma equilibrium control have been discussed in the chapters of this thesis. The conclusions obtained in each discussion are now summarized in this final chapter. Furthermore, a synthesis of plasma equilibrium control will be presented on the basis of the proposed methods and techniques.

V.1 Conclusions

As for tokamak plasma shape identification, two methods are proposed in Chapter II. The first method proposed in Chapter II.1, TOLFEX (toroidal-coordinates Legendre-Fourier expansion) method, is based on the analytical solution of Maxwell's equations in a vacuum using an infinite series of eigenfunctions. The following conclusions are obtained:

- (1) The method can identify the shape of an asymmetric divertor plasma without information on the expansion center (R_0, Z_0) because the point (R_0, Z_0) can be determined through "the two-step least squares method." It can also identify the shape of a small circular plasma.
- (2) By employing a discrete-point boundary condition and a finite series of flux eigenfunctions, the plasma shape can be accurately reproduced in application to JT-60 Upgrade.
- (3) The method can take eddy currents into consideration. Information of uniform field produced by the eddy currents is contained in the eigenfunctions having Legendre functions of the second kind.

However, the TOLFEX method cannot reproduce ITER (International Thermonuclear Experimental Reactor) plasmas. Then, the more mathematically-rigorous method based on the boundary integral equations (BIE) is next proposed in Chapter II.2. This BIE method is to solve the Maxwell's equations exterior to a plasma column using simultaneous boundary integral equations. The following conclusions are reached as a result of discussions in Chapter II.2.

- (1) A necessary condition to identify the shape of the plasma surface is that either flux intensities tangential to the curved surface $\partial\Omega_s$ or flux function

values at points on $\partial\Omega_s$ can be continuously given together with the complete knowledge of current density distribution in the region, except in the plasma. The sensor surface, $\partial\Omega_s$, is the closed curved surface along which the magnetic sensors are located. Knowledge of plasma internal quantities is essentially unnecessary for the shape identification.

- (2) The application of the BIE method to JT-60U ($\kappa \approx 1.5$) and ITER ($\kappa \approx 2.2$) shows that this method identifies the plasma shape more accurately even with a finite number of magnetic sensors along $\partial\Omega_s$. As this method is used to numerically compute the exact analytical solution of the concerned partial differential equation, and if the proper number of sensors are properly located along $\partial\Omega_s$, the shape is definitely and accurately reproduced independently of the size or shape of the tokamak. Furthermore, several test calculations by the BIE method shows this method is sufficiently practical.

As for modelling of tokamak plasma equilibrium dynamics, a simple model and a model for a finite element analysis are proposed in Chapter III. The results of the study in Chapter III.1 provide the following conclusions:

- (1) The $\mathbf{A}-\phi$ (\mathbf{A} and ϕ are the magnetic vector and scalar potentials, respectively) method with anisotropic conductivity can reproduce the evolution of the external field penetration into the JT-60 vessel. The penetration characteristics are determined by the bellows part. The penetration response is regarded as a system of a first-order differential equation.
- (2) The ITP (infinitely-thin-plate) and FCC (filament-current-coil) approximations for the vessel are not as accurate as the $\mathbf{A}-\phi$ method to simulate JT-60 operations.
- (3) The simplified ECD (equilibrium-control-dynamics) model can well reproduce the JT-60 position control. The parameters in the model can be determined by knowledge of the device available during the design phase. Thus, the model is able to be used for the design of the plasma feedback control system.
- (4) The plasma-vessel interaction is explained by the characteristic that the equilibrium force on the plasma is balanced, and the approximate relation, $\mathbf{B}_{\text{move}} = \mathbf{K} \cdot I_p \cdot \mathbf{v}_p$, (this equation signifies that the magnetic field induced by the plasma movement is proportional to the plasma current and the plasma velocity) holds in JT-60.

Formulation of coil-vessel-plasma electromagnetic interactions in a tokamak has been conducted and numerical methods (automatic mesh generation and large scale matrix algebra) have been developed for the finite element analysis in Chapter III.2. However, the method to determine the conductivity tensor and pressure profile in a plasma has not yet been developed. Even without this, the analysis for the nominal plasma will be possible, because the control system design needs to know the plasma electromagnetic behavior at the current flat top. Hence, this analysis can give a precise model for investigation of plasma control algorithms with the realistic conductivity and pressure evolutions.

As for tokamak plasma equilibrium systems, in Chapter IV, design and operation of JT-60 and JT-60 Upgrade plasma control systems using digital computers are discussed from the technological aspects of software and hardware in detail. In particular, how to build up a parallel and pipeline computer system is presented. Highly elongated JT-60U plasmas ($\kappa \sim 1.5$) are also stably controlled by the 250- μ sec cycle feedback control in recent experiments, where the expected performances are completely attained. It is shown that real-time shape visualization can be performed with the recent advancement of computer technology.

V.2 Synthesis of Tokamak Plasma Equilibrium Control

To build up a plasma equilibrium control system on the basis of the proposed methods and techniques, the following steps should be completed.

The zero-th step of design:

Before starting the design of control system, a tokamak device must be fixed, first of all.

- (a) Required plasma performances should be decided. Accordingly,
- (b) plasma static equilibrium configuration is determined using a plasma equilibrium code. There is no method to derive what plasma configuration will give the required performances. (It is still a big problem.)

These result in (1) the poloidal field (PF) coil locations are determined, and (2) figure, locations and materials of the vacuum vessel and other structural components are determined by rough estimations of heat and/or stress analysis.

The first step of design:

By utilizing the previously-determined design information, the following design activities can be initiated.

- (a) Plasma shape identification method is determined (refer to Chap. II). This makes it possible to determine the kinds and locations of electromagnetic sensors (refer to Chap. II.2). Furthermore, the required computation program steps can be estimated.
- (b) PF coil dynamics are roughly calculated.
- (c) Plasma-vessel-coil interactions can be modelled by the simple ECD (Equilibrium Control Dynamics) model (refer to Chap. III.1) or by the finite element electromagnetic model (refer to Chap. III.2). The simplest model (presented in Chap. IV.1) can also give rough estimation.

By simulating these models with various control algorithms, preferable control methods are chosen. This yields the requirements to the control system software/hardware specification.

The second step of design:

As all the specifications are fixed, the hardware/software design and construction begins (refer to Chap. IV). If necessary, parallel and/or pipeline processing may be taken into consideration.

After the hardware and software of the plasma control system is completed, the performance is evaluated in the test. The control system delays are measured. The actuators' dynamics is also tested by coil excitation test.

The coil current can be sinusoidally evolved. The system identification in the frequency domain can be conducted (refer to Chap. III.1). The interactions of the PF-coil with other components except a plasma are experimentally clarified.

At this stage, the accurate simple ECD model (refer to Chap. III.1) can be composed.

The third step of design:

Then the realistic controlled object, the simple ECD model and/or the finite element model, is established. By simulating the model, various control algorithms based on control theories can be examined. The optimality must be searched at this phase. If it is necessary to improve the performance of software/hardware, the design step is changed back to the second (or first) step.

A synthesis of tokamak plasma equilibrium control is obtained above. Several problems in this field have been discussed, but there still remains many unsolved problems in tokamak plasma behavior on the way to the goal — "the release of thermonuclear controlled fusion energy."

Major remaining problems are now pointed out from a view point of tokamak plasma control:

<Theoretical aspects> More sophisticated and systematic studies of plasma energy/particle transport should be strongly advanced. The relations of microscopic plasma particle behavior and macroscopic manipulation should be elucidated. It may require the new theoretical area of applied mathematics, computational physics or some other fields of science.

<Technological aspects> A faster computer with large memory area should be also strongly advanced. It may require parallel/pipelined processing by multiple computers. The processor hardware has been advancing to a certain level. But the software that enables the efficient production of programs for multiple processors, "compiler for parallel processing," is expected to be developed.

List of Publications Concerning This Thesis

Chapter II

- [1] Kurihara, K., "Improvement of the tokamak plasma shape identification with a Legendre-Fourier expansion of the vacuum poloidal flux function," Fusion Technology, Vol.21, No.11 (1992).
Kurihara, K., et al., "Tokamak plasma shape identification with a Legendre-Fourier expansion of the vacuum poloidal flux function," Japan Atomic Energy Research Institute Report, JAERI-M 90-001 (1990) (in Japanese)
- [2] Kurihara, K., "Tokamak plasma shape identification based on boundary integral equations," Submitted to Nuclear Fusion (July 1992).
Kurihara, K., et al., "Tokamak plasma shape identification based on boundary integral equations," JAERI-M 92-075 (1992) (in Japanese)
- [3] Kurihara, K., et al., "Tokamak plasma shape identification based on boundary integral equations and the real-time shape visualization system," Proceedings of 17th Symposium on Fusion Technology, Sept. 1992, Rome (Italy).
- [4] Wesley, J., Beljakov, V., Bulmer, R., Hogan, J.T., Kaiser, T.,Kavin, A., Korshakov, V., Kostenko, A., Kurihara, K., et al., "The ITER poloidal field system," Plasma Physics and Controlled Nuclear Fusion Research 1990 (IAEA-CN-53/F-III-16, Proc. 13th Int. Conf., Washington D.C., 1990), Vol.3, IAEA, Vienna, (1991) p.421.

Chapter III

- [1] Kurihara, K., "Eddy current effect study on JT-60 plasma equilibrium control," Fusion Engineering and Design, Vol.19, (1992) pp.235-257.
- [2] Kurihara, K., "Analytical solution on magnetic field penetration into an infinitely long cylindrical conductor," Submitted to the Japan Society for Industrial and Applied Mathematics (Feb. 1992) (in Japanese).

Chapter IV

Design of JT-60 and JT-60U control systems

- [1] Kurihara, K., et al., "JT-60 Plasma control system," Fusion Engineering and Design vol.11 (1990) pp.441-454.

- [2] Kurihara, K., et al., "System design for JT-60 failure mode analysis and prediction," Proceedings of 10th Symposium on Fusion Engineering, 1983, Philadelphia (USA).
- [3] Kurihara, K., et al., "System design for JT-60 computer aided production of preprogrammed waveforms," Proceedings of 13th Symposium on Fusion Technology, 1984, Varese (Italy).
- [4] Kurihara, K., et al., "Dynamics of plasma current control system in JT-60," Proceedings of 12th Symposium on Fusion Engineering, 1987, Monterey (USA).
- [5] Kurihara, K., et al., "JT-60 plasma control system," Proceedings of the first workshop on control systems, National Laboratory for High Energy Physics Report No. KEK 87-25, 1987, Tsukuba (Japan) pp.57-60.
- [6] Kimura, T., Kurihara, K., et al., "Application of the fast array processor for JT-60 plasma control," Proceedings of 14th Symposium on Fusion Technology, 1986, Avignon (France).
- [7] Kimura, T., Kurihara, K., et al., "VME multiprocessor system for plasma control at the JT-60 Upgrade," Proceedings of Real-Time '89, IEEE Transactions on Nuclear Science vol. 36, No. 5 (1989) pp.1554-1558.
- [8] Kawamata, Y., Kurihara, K., Kimura, T., Takahashi, M., "Tests on fast data transfer between a VME-bus system and a CAMAC system," JAERI-M 90-005 (1990) *(in Japanese)*

Control system design based on modern/classical control theories

- [9] Kurihara, K., Honda, M., Nakamura, Y., Kimura, T., "Program package for control system design and analysis (DPACS/J)," JAERI-M 89-126 (1989) *(in Japanese)*

Database system for plasma control analyses

- [10] Kurihara, K., Itoh, Y., Kimura, T., "JT-60 database system (I) — basic concept and system design," JAERI-M 87-097 (1987) *(in Japanese)*
- [11] Itoh, Y., Kurihara, K., Kimura, T., "JT-60 database system (II) — detailed design manual," JAERI-M 87-098 (1987) *(in Japanese)*
- [12] Yonekawa, I., Kurihara, K., Itoh, Y., Kimura, T., "Development of JT-60 database management system," Proceedings of 12th Symposium on Fusion Engineering, 1987, Monterey (USA).

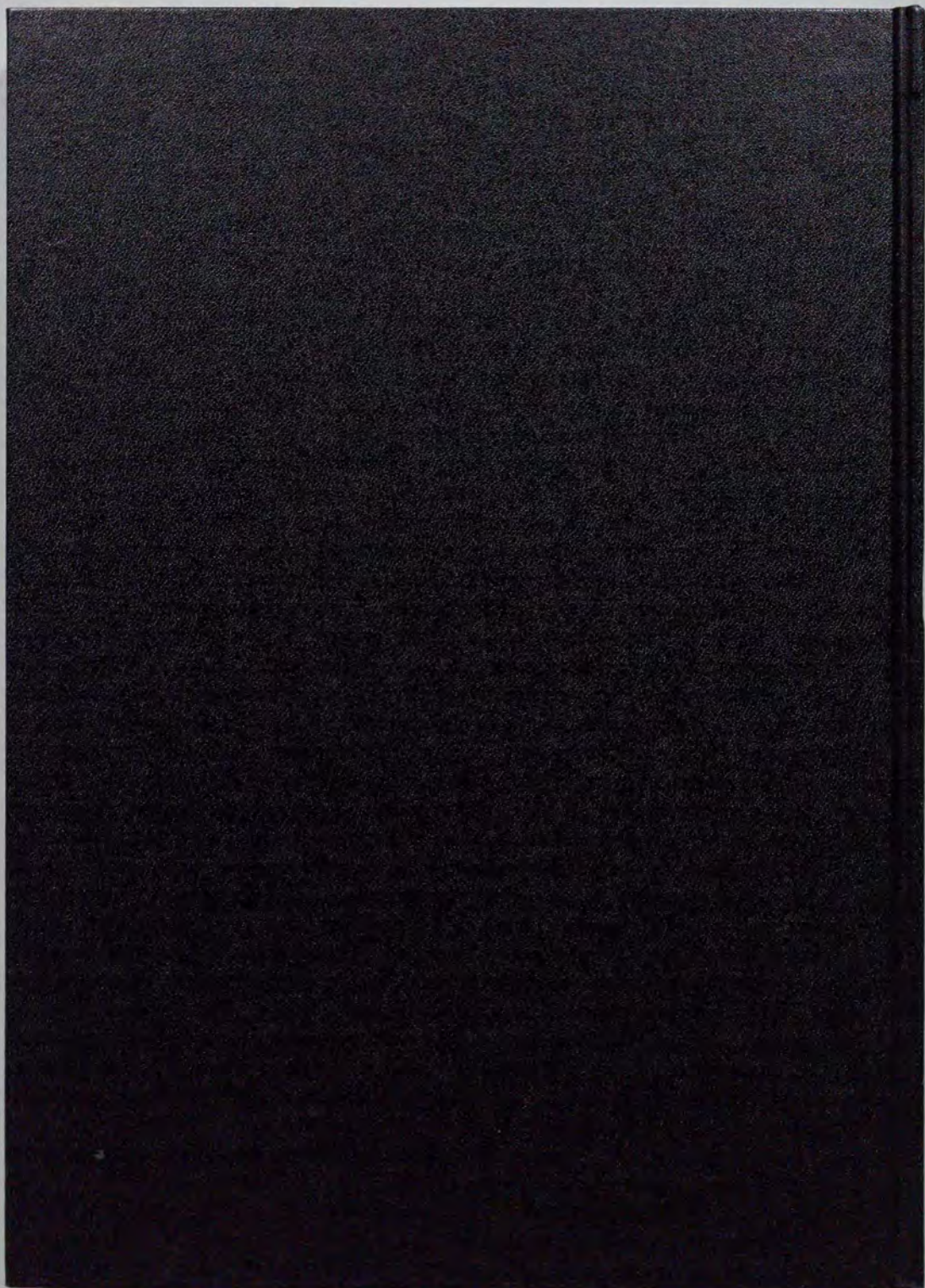
Acknowledgments

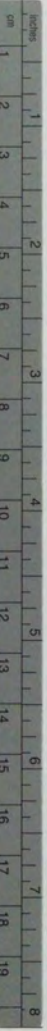
The author would like to express his appreciation to Professor N. Inoue of University of Tokyo for the continuous guidance and helpful suggestions. He also wishes to express his gratitude to Professor Y. Oka, Associated Professor Y. Ogawa and Associated Professor Z. Yoshida of University of Tokyo for their beneficial discussions and advice.

The author thanks Dr. T. Kimura of JAERI (JAERI: Japan Atomic Energy Research Institute) for many meaningful discussions, useful suggestions, much encouragement and continuous support.

He also expresses his gratitude to Drs. A. Ogata (National Laboratory for High Energy Physics) and H. Aikawa (JAERI), who stimulated the author to investigate plasma control, Dr. H. Ninomiya (JAERI), who prepared the JT-60U equilibrium code, Drs. Y. Shimomura and M. Sugihara (JAERI), who provided the opportunity for the author to consider an ITER poloidal system, Dr. K. Shinya (Toshiba Corp.), who executed the ITER equilibrium code, and Dr. M. G. Bell (PPPL: Princeton Plasma Physics Laboratory), who made helpful discussions and kind suggestions on plasma control systems when the author stayed in PPPL as a visiting researcher.

The author wishes to express his gratitude to Drs. I. Kondo (JAERI), M. Shimizu (JAERI), M. Ohta (JAERI) and Y. Tanaka (JAERI) for their continuous encouragement and support.





Kodak Color Control Patches

© Kodak, 2007 TM Kodak

Blue	Cyan	Green	Yellow	Red	Magenta	White	3/Color	Black
[Patch 1]	[Patch 2]	[Patch 3]	[Patch 4]	[Patch 5]	[Patch 6]	[Patch 7]	[Patch 8]	[Patch 9]

Kodak Gray Scale



© Kodak, 2007 TM Kodak

A 1 2 3 4 5 6 M 8 9 10 11 12 13 14 15 B 17 18 19

